Observation of the decay $B_s^0 \to \bar{D}^0 K^+ K^-$

R. Aaij *et al.*[*]

(LHCb Collaboration)

The first observation of the $B_s^0 \to \bar{D}^0 K^+ K^-$ decay is reported, together with the most precise branching fraction measurement of the mode $B^0 \to \bar{D}^0 K^+ K^-$. The results are obtained from an analysis of pp collision data corresponding to an integrated luminosity of 3.0 fb^{-1}. The data were collected with the LHCb detector at center-of-mass energies of 7 and 8 TeV. The branching fraction of the $B^0 \to \bar{D}^0 K^+ K^-$ decay is measured relative to that of the decay $B^0 \to \bar{D}^0 \pi^+ \pi^-$ to be $\frac{\mathcal{B}(B^0 \to \bar{D}^0 K^+ K^-)}{\mathcal{B}(B^0 \to \bar{D}^0 \pi^+ \pi^-)} = (6.9 \pm 0.4 \pm 0.3)\%$, where the first uncertainty is statistical and the second is systematic. The measured branching fraction of the $B_s^0 \to \bar{D}^0 K^+ K^-$ decay mode relative to that of the corresponding B^0 decay is $\frac{\mathcal{B}(B_s^0 \to \bar{D}^0 K^+ K^-)}{\mathcal{B}(B^0 \to \bar{D}^0 K^+ K^-)} = (93.0 \pm 8.9 \pm 6.9)\%$. Using the known branching fraction of $B^0 \to \bar{D}^0 \pi^+ \pi^-$, the values of $\mathcal{B}(B^0 \to \bar{D}^0 K^+ K^-) = (6.1 \pm 0.4 \pm 0.3 \pm 0.3) \times 10^{-5}$ and $\mathcal{B}(B_s^0 \to \bar{D}^0 K^+ K^-) = (5.7 \pm 0.5 \pm 0.4 \pm 0.5) \times 10^{-5}$ are obtained, where the third uncertainties arise from the branching fraction of the decay modes $B^0 \to \bar{D}^0 \pi^+ \pi^-$ and $B^0 \to \bar{D}^0 K^+ K^-$, respectively.

I. INTRODUCTION

The precise measurement of the angle γ of the Cabibbo-Kobayashi-Maskawa (CKM) unitarity triangle [1,2] is a central topic in flavor physics experiments. Its determination at the subdegree level in tree-level open-charm b-hadron decays is theoretically clean [3,4] and provides a standard candle for measurements sensitive to new physics effects [5]. In addition to the results from the B factories [6], various measurements from LHCb [7–9] allow the angle γ to be determined with an uncertainty of around 5°. However, no single measurement dominates the world average, as the most accurate measurements have an accuracy of about 10° to 20° [10,11]. Alternative methods are therefore important to improve the precision. Among them, an analysis of the decay $B_s^0 \to \bar{D}^0 \phi$ has the potential to make a significant impact [12–15]. Moreover, a Dalitz plot analysis of $B_s^0 \to \bar{D}^0 K^+ K^-$ decays can further improve the determination of γ due to the increased sensitivity to interference effects, as well as allowing the CP-violating phase ϕ_s to be determined in $B_s^0 - \bar{B}_s^0$ mixing with minimal theoretical uncertainties [16].

The mode $B_s^0 \to \bar{D}^0 \phi$ has been previously observed by the LHCb Collaboration with a data sample corresponding to an integrated luminosity of 1.0 fb^{-1} [17]. The observation of $B^0 \to \bar{D}^0 K^+ K^-$ and evidence for $B_s^0 \to \bar{D}^0 K^+ K^-$ have also been reported by the LHCb Collaboration using a data sample corresponding to 0.62 fb^{-1} [18]. These decays are mediated by decay processes such as those shown in Fig. 1.

In this paper an improved measurement of the branching fraction of the decay $B^0 \to \bar{D}^0 K^+ K^-$ and the first observation of the decay $B_s^0 \to \bar{D}^0 K^+ K^-$ are presented.[1] The branching fractions are measured relative to that of the topologically similar and abundant decay $B^0 \to \bar{D}^0 \pi^+ \pi^-$. The analysis is based on a data sample corresponding to an integrated luminosity of 3.0 fb^{-1} of pp collisions collected with the LHCb detector. Approximately one third of the data was obtained during 2011, when the collision center-of-mass energy was $\sqrt{s} = 7$ TeV, and the rest during 2012 with $\sqrt{s} = 8$ TeV. Compared to the previous analysis [18], a revisited selection and a more sophisticated treatment of the various background sources are employed, as well as improvements in the handling of reconstruction and trigger efficiencies, leading to an overall reduction of systematic uncertainties. The present analysis benefits from the improved knowledge of the decays $B_{(s)}^0 \to \bar{D}^0 K^- \pi^+$ [19], $\Lambda_b^0 \to D^0 p h^-$, where h^- stands for a π^- or a K^- meson [20], which contribute to the background, and of the normalization decay mode $B^0 \to \bar{D}^0 \pi^+ \pi^-$ [21].

[*]Full author list given at the end of the article.

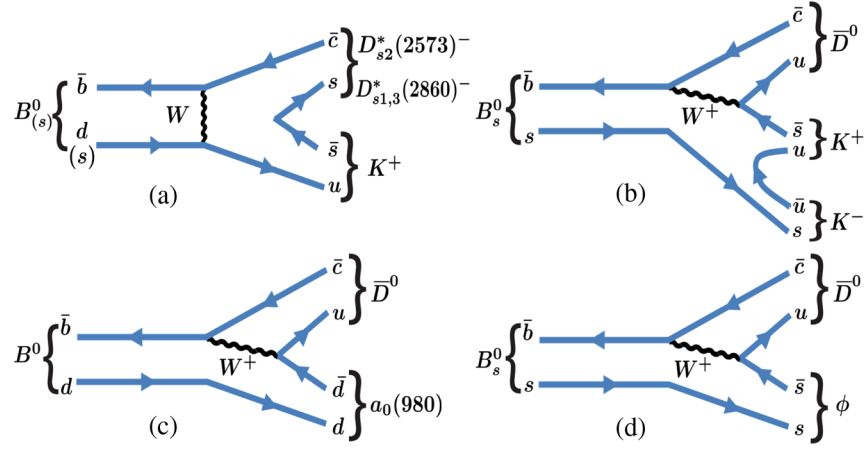[1]The inclusion of charge conjugate modes is implied throughout this paper.

FIG. 1.   Example Feynman diagrams that contribute to the $B^0_{(s)} \to \bar{D}^0 K^+ K^-$ decays via (a) W-exchange, (b) nonresonant three body mode, (c),(d) rescattering from a color-suppressed decay.

This analysis sets the foundation for the study of the $B^0_{(s)} \to \bar{D}^{(*)0}\phi$ decays, which are presented in a separate publication [22]. The current data set does not yet allow a Dalitz plot analysis of the $B^0_{(s)} \to \bar{D}^0 K^+ K^-$ decays to be performed, but these modes could provide interesting input to excited D^+_s meson spectroscopy, in particular because the decay diagrams are different from those of the $B^0_s \to \bar{D}^0 K^- \pi^+$ decay [23] (i.e., different resonances can be favored in each decay mode).

This paper is structured as follows. A brief description of the LHCb detector, as well as the reconstruction and simulation software, is given in Sec. II. Signal selection and background suppression strategies are summarized in Sec. III. The characterization of the various remaining backgrounds and their modeling is described in Sec. IV and the fit to the $B^0 \to \bar{D}^0 \pi^+ \pi^-$ and $B^0_{(s)} \to \bar{D}^0 K^+ K^-$ invariant-mass distributions to determine the signal yields is presented in Sec. V. The computation of the efficiencies needed to derive the branching fractions is explained in Sec. VI and the evaluation of systematic uncertainties is described in Sec. VII. The results on the branching fractions and a discussion of the Dalitz plot distributions are reported in Sec. VIII.

II. DETECTOR AND SIMULATION

The LHCb detector [24,25] is a single-arm forward spectrometer covering the pseudorapidity range $2 < \eta < 5$, designed for the study of particles containing b or c quarks. The detector includes a high-precision tracking system consisting of a silicon-strip vertex detector surrounding the pp interaction region [26], a large-area silicon-strip detector located upstream of a dipole magnet with a bending power of about 4 Tm, and three stations of silicon-strip detectors and straw drift tubes [27] placed downstream of the magnet. The tracking system provides a measurement of momentum, p, of charged particles with a relative

uncertainty that varies from 0.5% at low momentum to 1.0% at 200 GeV/c. The minimum distance of a track to a primary vertex (PV), the impact parameter (IP), is measured with a resolution of $(15 + 29/p_T)$ μm, where p_T is the component of the momentum transverse to the beam, in GeV/c. Different types of charged hadrons are distinguished using information from two ring-imaging Cherenkov (RICH) detectors [28]. Photons, electrons, and hadrons are identified by a calorimeter system consisting of scintillating-pad and preshower detectors, an electromagnetic calorimeter, and a hadronic calorimeter. Muons are identified by a system composed of alternating layers of iron and multiwire proportional chambers [29].

The online event selection is performed by a trigger, which consists of a hardware stage, based on information from the calorimeter and muon systems, followed by a software stage, which applies a full event reconstruction. At the hardware trigger stage, events are required to have a muon with high p_T or a hadron, photon, or electron with high transverse energy in the calorimeters. For hadrons, the transverse energy threshold is 3.5 GeV. A global hardware trigger decision is ascribed to the reconstructed candidate, the rest of the event or a combination of both; events triggered as such are defined respectively as triggered on signal (TOS), triggered independently of signal (TIS), and triggered on both. The software trigger requires a two-, three-, or four-track secondary vertex with a significant displacement from the primary pp interaction vertices. At least one charged particle must have a transverse momentum $p_T > 1.7$ GeV/c and be inconsistent with originating from a PV. A multivariate algorithm [30] is used for the identification of secondary vertices consistent with the decay of a b hadron.

Candidates that are consistent with the decay chain $B^0_{(s)} \to \bar{D}^0 K^+ K^-$, $\bar{D}^0 \to K^+ \pi^-$ are selected. In order to reduce systematic uncertainties in the measurement, the topologically similar decay $B^0 \to \bar{D}^0 \pi^+ \pi^-$, which has

previously been studied precisely [21,31], is used as a normalization channel. Tracks are required to be consistent with either the kaon or pion hypothesis, as appropriate, based on particle identification (PID) information from the RICH detectors. All other selection criteria are tuned on the $B^0 \to \bar{D}^0 \pi^+ \pi^-$ channel. The large yields available in the normalization sample allow the selection to be based on data. Simulated samples, generated uniformly over the Dalitz plot, are used to evaluate efficiencies and characterize the detector response for signal and background decays. In the simulation, pp collisions are generated using PYTHIA [32] with a specific LHCb configuration [33]. Decays of hadronic particles are described by EVTGEN [34], in which final-state radiation is generated using PHOTOS [35]. The interaction of the generated particles with the detector, and its response, are implemented using the GEANT4 toolkit [36] as described in Ref. [37].

III. SELECTION CRITERIA AND REJECTION OF BACKGROUNDS

A. Initial selection

Signal $B^0_{(s)}$ candidates are formed by combining $\bar{D}^0$ candidates, reconstructed in the decay channel $K^+ \pi^-$, with two additional tracks of opposite charge. After the trigger, an initial selection, based on kinematic and topological variables, is applied to reduce the combinatorial background by more than two orders of magnitude. This selection is designed using simulated $B^0 \to \bar{D}^0 \pi^+ \pi^-$ decays as a proxy for signal and data $B^0 \to \bar{D}^0 \pi^+ \pi^-$ candidates lying in the upper-mass sideband [5400, 5600] MeV/c^2 as a background sample. The combinatorial background arises from random combinations of tracks that do not come from a single decay. For the $B^0 \to \bar{D}^0 \pi^+ \pi^-$ mode, no b-hadron decay contribution is expected in the upper sideband [5320, 6000] MeV/c^2, i.e., no B^0_s contribution is expected [38].

The reconstructed tracks are required to be inconsistent with originating from any PV. The $\bar{D}^0$ decay products are required to originate from a common vertex with an invariant mass within ± 25 MeV/c^2 of the known $\bar{D}^0$ mass [39]. The invariant-mass resolution of the reconstructed $\bar{D}^0$ mesons is about 8 MeV/c^2 and the chosen invariant-mass range allows most of the background from the $\bar{D}^0 \to K^+ K^-$ and $\bar{D}^0 \to \pi^+ \pi^-$ decays to be rejected. The $\bar{D}^0$ candidates and the two additional tracks are required to form a vertex. The reconstructed $\bar{D}^0$ and B^0 vertices must be significantly displaced from the associated PV, defined, in case of more than one PV in the event, as that which has the smallest χ^2_{IP} with respect to the B candidate. The χ^2_{IP} is defined as the difference in the vertex-fit quality χ^2 of a given PV reconstructed with and without the particle under consideration. The reconstructed $\bar{D}^0$ vertex is required to be displaced downstream from the reconstructed $B^0_{(s)}$ vertex, along the beam axis direction. This requirement reduces the

background from charmless B decays, corresponding to genuine $B^0 \to K^+ \pi^- h^+ h^-$ decays, for instance from $B^0 \to K^+ \pi^- \rho^0$ or $B^0 \to K^{*0} \phi$ decays, to a negligible level. This requirement also suppresses background from prompt charm production, as well as fake reconstructed $\bar{D}^0$ coming from the PV. The $B^0_{(s)}$ momentum vector and the vector connecting the PV to the $B^0_{(s)}$ vertex are requested to be aligned.

Unless stated otherwise, a kinematic fit [40] is used to improve the invariant-mass resolution of the $B^0_{(s)}$ candidate. In this fit, the $B^0_{(s)}$ momentum is constrained to point back to the PV and the $\bar{D}^0$-candidate invariant mass to be equal to its known value [39], and the charged tracks are assigned the K or π mass hypothesis as appropriate. Only $B^0_{(s)} \to \bar{D}^0 h^+ h^-$ candidates with an invariant mass ($m_{\bar{D}^0 h^+ h^-}$) within the range [5115, 6000] MeV/c^2 are then considered. This range allows the $B^0_{(s)}$ signal regions to be studied, while retaining a sufficiently large upper sideband to accurately determine the invariant-mass shape of the surviving combinatorial background. The lower-mass limit removes a large part of the complicated partially reconstructed backgrounds and has a negligible impact on the determination of the signal yields.

The world-average value of the branching fraction $\mathcal{B}(B^0 \to \bar{D}^0 \pi^+ \pi^-)$ is equal to $(8.8 \pm 0.5) \times 10^{-4}$ [39] and is mainly driven by the Belle [31] and LHCb [21] measurements. This value is used as a reference for the measurement of the branching fractions of the decays $B^0_{(s)} \to \bar{D}^0 K^+ K^-$. The large contribution from the exclusive decay chain $B^0 \to D^*(2010)^- \pi^+$, $D^*(2010)^- \to \bar{D}^0 \pi^-$, with a branching fraction of $(1.85 \pm 0.09) \times 10^{-3}$ [39], is not included in the above value. Thus, a $D^*(2010)^-$ veto is applied. The veto consists of rejecting candidates with $m_{\bar{D}^0 \pi^-} - m_{\bar{D}^0}$ within ± 4.8 MeV/c^2 of the expected mass difference [39], which corresponds to ± 6 times the LHCb detector resolution on this quantity. Due to its high production rate and possible misidentification of its decay products, the decay $B^0 \to D^*(2010)^-(\to \bar{D}^0 \pi^-) \pi^+$ could also contribute as a background to the $B^0_{(s)} \to \bar{D}^0 K^+ K^-$ channel. Therefore, the same veto criterion is applied to $B^0_{(s)} \to \bar{D}^0 K^+ K^-$ candidates as for the $B^0 \to \bar{D}^0 \pi^+ \pi^-$ normalization mode, where the invariant mass difference $m_{\bar{D}^0 \pi^-} - m_{\bar{D}^0}$ is computed after assigning the pion mass to each kaon in turn.

Only kaon and pion candidates within the kinematic region corresponding to the fiducial acceptance of the RICH detectors [28] are kept for further analysis. This selection is more than 90% efficient for the $B^0 \to \bar{D}^0 \pi^+ \pi^-$ signal, as estimated from simulation. Although the $\bar{D}^0$ candidates are selected in a narrow mass range, studies on simulated samples show a small fraction of $\bar{D}^0 \to K^+ K^-$ ($\sim 4.5 \times 10^{-5}$) and $\bar{D}^0 \to \pi^+ \pi^-$ ($\sim 3.0 \times 10^{-4}$) decays, with respect to the genuine $\bar{D}^0 \to K^+ \pi^-$ signal, are still selected.

Therefore, loose PID requirements are applied in order to further suppress $\bar{D}^0 \to K^+K^-$ and $\bar{D}^0 \to \pi^+\pi^-$ decays. In the doubly Cabibbo-suppressed $D^0 \to K^+\pi^-$ decay both the kaon and the pion are correctly identified and reconstructed, but the $\bar{D}^0$ flavor is misidentified. This is expected to occur in less than $R_D = (0.348^{+0.004}_{-0.003})\%$ [7] of $\bar{D}^0 \to K^+\pi^-$ signal decays. However, such an effect does not impact the measurements of the ratio of branching fractions $\mathcal{B}(B^0 \to \bar{D}^0K^+K^-)/\mathcal{B}(B^0 \to \bar{D}^0\pi^+\pi^-)$ and $\mathcal{B}(B^0_s \to \bar{D}^0K^+K^-)/\mathcal{B}(B^0 \to \bar{D}^0K^+K^-)$, as the resulting dilution is the same for the numerator and the denominator.

B. Multivariate selection

Once the initial selections are implemented, a multivariate analysis (MVA) is applied to further discriminate between signal and combinatorial background. The implementation of the MVA is performed with the TMVA package [41,42], using the $B^0 \to \bar{D}^0\pi^+\pi^-$ normalization channel to optimize the selection. For this purpose only, a loose PID criterion on the pions of the $\pi^+\pi^-$ pair is set to reject the kaon and proton hypotheses. The *sPlot* technique [43] is used to statistically separate signal and background in data, with the B^0 candidate invariant mass used as the discriminating variable. The *sPlot weights* (*sWeights*) obtained from this procedure are applied to the candidates to obtain signal and background distributions that are then used to train the discriminant.

To compute the *sWeights*, the signal- and combinatorial-background yields are determined using an unbinned extended maximum-likelihood fit to the invariant-mass distribution of B^0 candidates. The fit uses the sum of a crystal ball (CB) function [44] and a Gaussian function for the signal distribution and an exponential function for the combinatorial background distribution. The fit is first performed in the invariant-mass range $m_{\bar{D}^0\pi^+\pi^-} \in$ $[5240, 5420]$ MeV/c^2, to compute the *sWeights*, and is repeated within the signal region $[5240, 5320]$ MeV/c^2 with all the parameters fixed to the result of the initial fit, except the signal and the background yields, which are found to be 44690 ± 540 and 81710 ± 570, respectively. The training samples are produced by applying the necessary signal and background *sWeights*, with half of the data used and randomly chosen for training and the other half for validation.

Several sets of discriminating variables, as well as various linear and nonlinear MVA methods, are tested. These variables contain information about the topology and the kinematic properties of the event, vertex quality, χ^2_{IP} and p_T of the tracks, track multiplicity in cones around the B^0 candidate, relative flight distances between the B^0 and $\bar{D}^0$ vertices and from the PV. All of the discriminating variables have weak correlations ($<1.6\%$) with the invariant mass $m_{\bar{D}^0\pi^+\pi^-}$ of the B^0 candidates. Very similar separation

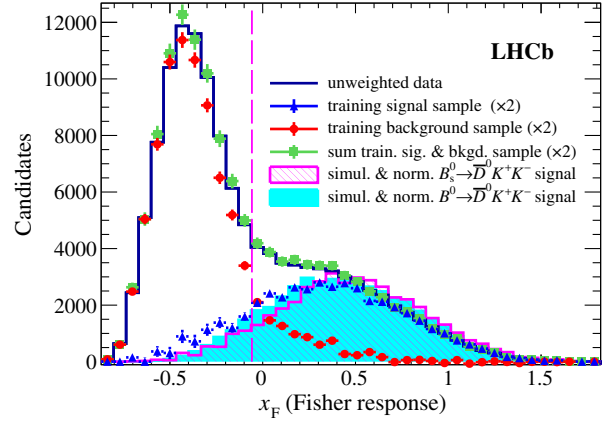FIG. 2. Distributions of the Fisher discriminant, for preselected $B^0 \to \bar{D}^0\pi^+\pi^-$ data candidates, in the mass range $[5240, 5320]$ MeV/c^2: (black line) unweighted data distribution, and *sWeighted* training samples: (blue triangles) signal, (red circles) background, and (green squares) their sum. The training samples are scaled with a factor of two to match the total yield. The cyan (magenta) filled (hatched) histogram displays the simulated $B^0(B^0_s) \to \bar{D}^0K^+K^-$ decay signal candidates that are normalized to the number of $B^0 \to \bar{D}^0\pi^+\pi^-$ normalization channel candidates (blue triangles). The (magenta) vertical dashed line indicates the position of the nominal selection requirement.

performance is seen for all the tested discriminants. Therefore, a Fisher discriminant [45] with the minimal set of the five most discriminating variables is adopted as the default MVA configuration. This option is insensitive to overtraining effects. These five variables are the smallest values of χ^2_{IP} and p_T for the tracks of the $\pi^+\pi^-$ pair, flight distance significance of the reconstructed B^0 candidates, the $D\chi^2_{\text{IP}}$, and the signed minimum cosine of the angle between the direction of one of the pions from the B decay and the $\bar{D}^0$ meson, as projected in the plane perpendicular to the beam axis.

Figure 2 shows the distributions of the Fisher discriminant for the *sWeighted* training samples (signal and background) and their sum, compared to the data set of preselected $B^0 \to \bar{D}^0\pi^+\pi^-$ candidates. These distributions correspond to candidates in the invariant-mass signal region, and agree well within the statistical uncertainties, demonstrating that no overtraining is observed. Based on the fitted numbers of signal and background candidates, the statistical figure of merit $Q = N_S/\sqrt{N_S + N_B}$ is defined to find an optimal operation point, where N_S and N_B are the numbers of selected signal and background candidates above a given value x_F of the Fisher discriminant. The value of x_F that maximizes Q is found to be -0.06, as shown in Fig. 2 and at this working point the signal efficiency is $(82.4 \pm 0.4)\%$ and the fraction of rejected background is $(89.2 \pm 1.0)\%$. In Fig. 2 the distribution of simulated $B^0(B^0_s) \to \bar{D}^0K^+K^-$ signal decays is also shown to be in

good agreement with the *sWeighted* $B^0 \to \bar{D}^0 \pi^+ \pi^-$ data training sample.

C. Particle identification of $h^+ h^-$ pairs

After the selections, specific PID requirements are set to identify the tracks of the $B^0_{(s)}$ decays to distinguish the normalization channel $B^0 \to \bar{D}^0 \pi^+ \pi^-$ and the $B^0_{(s)} \to \bar{D}^0 K^+ K^-$ signal modes. For the $B^0 \to \bar{D}^0 \pi^+ \pi^-$ normalization channel, the $\pi^{\pm}$ candidates must each satisfy the same PID requirements to identify them as pions, while the kaon and proton hypotheses are rejected. These criteria are tuned by comparing a simulated sample of $B^0 \to \bar{D}^0 \pi^+ \pi^-$ signal and a combination of simulated samples that model the misidentified backgrounds. The combination of backgrounds contains all sources expected to give the largest contributions, namely the $B^0 \to \bar{D}^0 K^+ K^-$, $B^0_s \to \bar{D}^0 K^+ K^-$, $B^0 \to \bar{D}^0 K^+ \pi^-$, $B^0_s \to \bar{D}^0 K^- \pi^+$, $\Lambda^0_b \to D^0 p \pi^-$, and $\Lambda^0_b \to D^0 p K^-$ decays. The same tuning procedure is repeated for the two $B^0_{(s)} \to \bar{D}^0 K^+ K^-$ signal modes, where the model for the misidentified background is composed of the main contributing background decays: $B^0 \to \bar{D}^0 \pi^+ \pi^-$, $B^0 \to \bar{D}^0 K^+ \pi^-$, $B^0_s \to \bar{D}^0 K^- \pi^+$, $\Lambda^0_b \to D^0 p \pi^-$, and $\Lambda^0_b \to D^0 p K^-$. The $K^{\pm}$ candidates are required to be positively identified as kaons and the pion and proton hypotheses are excluded. Loose PID requirements are chosen in order to favor the highest signal efficiencies and to limit possible systematic uncertainties due to data and simulation discrepancies arise when computing signal efficiencies related to PID (see Sec. VI).

D. Multiple candidates

Given the selection described above, 1.2% and 0.8% of the events contain more than one candidate in the $B^0 \to \bar{D}^0 \pi^+ \pi^-$ normalization and the $B^0_{(s)} \to \bar{D}^0 K^+ K^-$ signal modes, respectively. There are two types of multiple candidates to consider. In the first type, for which two or more good B or D decay vertices are present, the candidate with the smallest sum of the $B^0_{(s)}$ and $\bar{D}^0$ vertex χ^2 is then kept. In the second type, which occurs if a swap of the mass hypotheses of the D decay products leads to a good candidate, the PID requirements for the two options $K^+ \pi^-$ and $\pi^+ K^-$ are compared and the candidate corresponding to the configuration with the highest PID probability is kept. In order no to bias the $m_{\bar{D}^0 h^+ h^-}$ invariant-mass distribution with the choice of the best candidate, it is checked with simulation that the variables used for selection are uncorrelated with the invariant mass, $m_{\bar{D}^0 h^+ h^-}$. It is also computed with simulation that differences between the efficiencies while choosing the best candidate for $B^0 \to \bar{D}^0 \pi^+ \pi^-$ and $B^0_{(s)} \to \bar{D}^0 K^+ K^-$ decays are negligible [46].

IV. FIT COMPONENTS AND MODELING

A. Background characterization

The $B^0_{(s)} \to \bar{D}^0 h^+ h^-$ selected candidates consist of signal and various background contributions: combinatorial, misidentified, and partially reconstructed b-hadron decays.

The misidentified background originates from real b-hadron decays, where at least one final-state particle is incorrectly identified in the decay chain. For the $B^0 \to \bar{D}^0 \pi^+ \pi^-$ normalization channel, three decays requiring a dedicated modeling are identified: $B^0 \to \bar{D}^0 K^+ \pi^-$, $B^0_s \to \bar{D}^0 K^- \pi^+$, and $\Lambda^0_b \to D^0 p \pi^-$. Due to the PID requirements, the expected contributions from $B^0_{(s)} \to \bar{D}^0 K^+ K^-$ are negligible. For the $B^0_{(s)} \to \bar{D}^0 K^+ K^-$ channels, the modes of interest are $B^0 \to \bar{D}^0 K^+ \pi^-$, $B^0_s \to \bar{D}^0 K^- \pi^+$, $\Lambda^0_b \to D^0 p K^-$, and $\Lambda^0_b \to D^0 p \pi^-$. Here as well, the contribution from $B^0 \to \bar{D}^0 \pi^+ \pi^-$ is negligible, due to the positive identification of both kaons. Using the simulation and recent measurements for the various branching fractions [18–21,39,47] and for the fragmentation factors f_s/f_d [48] and $f_{\Lambda^0_b}/f_d$ [49], an estimation of the relative yields with respect to those of the simulated signals is computed over the whole invariant-mass range, $m_{\bar{D}^0 h^+ h^-} \in [5115, 6000]$ MeV/c^2. The values are listed in Table I. The expected yields of the backgrounds related to decays of Λ^0_b baryons cannot be predicted accurately due the limited knowledge of their branching fractions and of the relative production rate $f_{\Lambda^0_b}/f_d$ [49].

The partially reconstructed background corresponds to real b-hadron decays, where a neutral particle is not reconstructed and possibly one of the other particles is misidentified. For example, $B^0_{(s)} \to \bar{D}^{*0} h^+ h^-$ decays with $\bar{D}^{*0} \to \bar{D}^0 \gamma$ or $\bar{D}^{*0} \to \bar{D}^0 \pi^0$, where the photon or the neutral pion is not reconstructed. This type of background populates the low-mass region $m_{\bar{D}^0 h^+ h^-} < 5240$ MeV/c^2.

TABLE I. Relative yields, in percent, of the various exclusive b-hadron decay backgrounds with respect to that of the $B^0 \to \bar{D}^0 \pi^+ \pi$ and $B^0_{(s)} \to \bar{D}^0 K^+ K^-$ signal modes. These relative contributions are estimated with simulation in the range $m_{\bar{D}^0 h^+ h^-} \in [5115, 6000]$ MeV/c^2.

Fraction [%]	$B^0 \to \bar{D}^0 \pi^+ \pi^-$	$B^0_{(s)} \to \bar{D}^0 K^+ K^-$
$B^0 \to \bar{D}^0 K^+ \pi^-$	1.3 ± 0.2	2.7 ± 0.7
$B^0_s \to \bar{D}^0 K^- \pi^+$	3.7 ± 0.7	8.1 ± 2.2
$\Lambda^0_b \to D^0 p \pi^-$	3.0 ± 2.8	1.6 ± 1.7
$\Lambda^0_b \to D^0 p K^-$	$\cdots$	5.6 ± 5.4
$B^0_s \to \bar{D}^{*0} K^- \pi^+$	1.8 ± 0.4	8.4 ± 2.9
$B^0 \to \bar{D}^{*0}[\bar{D}^0 \gamma]\pi^+ \pi^-$	16.9 ± 2.7	$\cdots$
$B^0_s \to \bar{D}^{*0}[\bar{D}^0 \pi^0]K^+ K^-$	$\cdots$	12.8 ± 6.7
$B^0_s \to \bar{D}^{*0}[\bar{D}^0 \gamma]K^+ K^-$	$\cdots$	5.5 ± 2.9

For the fit of the $B^0 \to \bar{D}^0 \pi^+ \pi^-$ invariant-mass distribution, the main contributions that need special treatment are $B_s^0 \to \bar{D}^{*0} K^- \pi^+$ and $B^0 \to \bar{D}^{*0} [\bar{D}^0 \gamma] \pi^+ \pi^-$, for which the branching fractions are poorly known [50]. For the $B_{(s)}^0 \to \bar{D}^0 K^+ K^-$ channels, the decays $B_s^0 \to \bar{D}^{*0} K^- \pi^+$ and $B_s^0 \to \bar{D}^{*0} [\bar{D}^0 \pi^0 / \gamma] K^+ K^-$ are of relevance. Using simulation and the available information on the branching fractions [39], and by making the assumption that $\mathcal{B}(B_s^0 \to \bar{D}^{*0} K^- \pi^+)$ and $\mathcal{B}(B_s^0 \to \bar{D}^0 K^- \pi^+)$ are equal (this is approximately the case for $B^0 \to \bar{D}^{*0} \pi^+ \pi^-$ and $B^0 \to \bar{D}^0 \pi^+ \pi^-$ decays), an estimate of the relative yields with respect to those of the simulated signals is computed over the whole invariant-mass range, $m_{\bar{D}^0 h^+ h^-} \in [5115, 6000]$ MeV/c^2. The values are given in Table I. The contributions from these backgrounds are somewhat larger than those of the misidentified background, but are mainly located in the mass region $m_{\bar{D}^0 h^+ h^-} < 5240$ MeV/c^2.

B. Signal modeling

The invariant-mass distribution for each of the signal $B_{(s)}^0 \to \bar{D}^0 h^+ h^-$ modes is parametrized with a probability density function (PDF) that is the sum of two CB functions with a common mean,

$$\begin{aligned} \mathcal{P}_{\text{sig}}(m) &= f_{\text{CB}} \times \text{CB}(m; m_0, \sigma_1, \alpha_1, n_1) \\ &\quad + (1 - f_{\text{CB}}) \times \text{CB}(m; m_0, \sigma_2, \alpha_2, n_2). \end{aligned} \quad (1)$$

The parameters $\alpha_{1,2}$ and $n_{1,2}$ describing the tails of the CB functions are fixed to the values fitted on simulated samples generated uniformly (phase space) over the $B_{(s)}^0 \to \bar{D}^0 h^+ h^-$ Dalitz plot. The mean value m_0, the resolutions σ_1 and σ_2, and the fraction f_{CB} between the two CB functions are free to vary in the fit to the $B^0 \to \bar{D}^0 \pi^+ \pi^-$ normalization channel. For the fit to $B_{(s)}^0 \to \bar{D}^0 K^+ K^-$ data, the resolutions σ_1 and σ_2 are fixed to those obtained with the normalization channel, while the mean value m_0 and the relative fraction f_{CB} of the two CB functions are left free. For $B_s^0 \to \bar{D}^0 K^+ K^-$ decays, the same function as for $B^0 \to \bar{D}^0 K^+ K^-$ is used; the mean values are free but the mass difference between B_s^0 and B^0 is fixed to the known value, $\Delta m_B = 87.35 \pm 0.23$ MeV/c^2 [39].

C. Combinatorial background modeling

For all channels, the combinatorial background contributes to the full invariant-mass range. It is modeled with an exponential function where the slope a_{comb} and the normalization parameter N_{comb} is free to vary in the fit. The invariant-mass range extends up to 6000 MeV/c^2 to include the region dominated by combinatorial background. This helps to constrain the combinatorial background yield and slope.

D. Misidentified and partially reconstructed background modeling

The shape of misidentified and partially reconstructed components is modeled by nonparametric PDFs built from large simulation samples. These shapes are determined using the kernel estimation technique [51]. The normalization of each component is free in the fits. For the normalization channel $B^0 \to \bar{D}^0 \pi^+ \pi^-$, a component for the decay $B^0 \to \bar{D}^{*0} [\bar{D}^0 \pi^0] \pi^+ \pi^-$ is added and modeled by a Gaussian distribution. This PDF also accounts for a possible contribution from the $B^+ \to \bar{D}^0 \pi^+ \pi^+ \pi^-$ decay, which has a similar shape. In the case of the $B_{(s)}^0 \to \bar{D}^0 K^+ K^-$ signal channels, the low-mass background also includes a Gaussian distribution to model the decay $B^0 \to \bar{D}^{*0} K^+ K^-$. To account for differences between data and simulation, these PDFs are modified to match the width and mean of the $m_{\bar{D}^0 \pi^+ \pi^-}$ distribution seen in the data. The normalization parameter, $N_{\text{Low}-m}$, of these partially reconstructed backgrounds is free to vary in the fit.

E. Specific treatment of the $\Lambda_b^0 \to D^0 p \pi^-$, $\Lambda_b^0 \to D^0 p K^-$, and $\Xi_b^0 \to D^0 p K^-$ backgrounds

Studies with simulation show that the distributions of the $\Lambda_b^0 \to D^0 p \pi^-$ and $\Lambda_b^0 \to D^0 p K^-$ background modes are broad below the $B_{(s)}^0 \to \bar{D}^0 h^+ h^-$ signal peaks. Although their branching fractions have been recently measured [20], the broadness of these backgrounds impacts the determination of both the $B^0 \to \bar{D}^0 h^+ h^-$ and the $B_s^0 \to \bar{D}^0 h^+ h^-$ signal yields. In particular, knowledge of the $\Lambda_b^0 \to D^0 p K^-$ background affects the $B_s^0 \to \bar{D}^0 K^+ K^-$ signal yield determination. The yields of these modes can be determined in data by assigning the proton mass to the h^- track of the $B_{(s)}^0 \to \bar{D}^0 h^+ h^-$ decay, where the charge of $h^\pm$ is chosen such that it corresponds to the Cabibbo-favored $\bar{D}^0$ mode in the $\Lambda_b^0 \to D^0 p h^-$ decay.

The invariant-mass distribution of $\Lambda_b^0 \to D^0 p \pi^-$ is obtained from the $B^0 \to \bar{D}^0 \pi^+ \pi^-$ candidates. A Gaussian distribution is used to model the $\Lambda_b^0 \to D^0 p \pi^-$ signal, while an exponential distribution is used for the combinatorial background. The validity of the background modeling is checked by assigning the proton mass hypothesis to the pion of opposite charge to that expected in the B^0 decay. Different fit regions are tested, as well as an alternative fit, where the resolution of the Gaussian PDF that models the $\Lambda_b^0 \to D^0 p \pi^-$ mass distribution is fixed to that of $B^0 \to \bar{D}^0 \pi^+ \pi^-$. The relative variations of the various configurations are compatible within their uncertainties; the largest deviations are used as the systematic uncertainties. Finally, the obtained yield for $\Lambda_b^0 \to D^0 p \pi^-$ is 1101 ± 144, including the previously estimated systematic uncertainties. This yield is then used as a Gaussian

TABLE II.   Fitted yields that are used as Gaussian constraints in the fit to the $B^0_{(s)} \to \bar{D}^0 h^+ h^-$ invariant-mass distributions presented in Sec. V B.

Mode	$B^0 \to \bar{D}^0 \pi^+ \pi^-$	$B^0_{(s)} \to \bar{D}^0 K^+ K^-$
$\Lambda^0_b \to D^0 p \pi^-$	1101 ± 144	74 ± 32
$\Lambda^0_b \to D^0 p K^-$	$\cdots$	193 ± 44
$\Xi^0_b \to D^0 p \pi^-$	$\cdots$	64 ± 21

constraint in the fit to the $m_{\bar{D}^0 \pi^+ \pi^-}$ invariant-mass distribution presented in Sec. V B and the fit results are presented in Table II.

The corresponding $m_{D^0 p K^-}$ and $m_{D^0 p \pi^-}$ distributions are determined using the $B^0_{(s)} \to \bar{D}^0 K^- K^+$ data set. Five components are used to describe the data and to fit the two distributions simultaneously: $\Lambda^0_b \to D^0 p K^-$, $\Xi^0_b \to D^0 p K^-$, $\Lambda^0_b \to D^0 p \pi^-$, $B^0_s \to \bar{D}^0 K^- \pi^+$, and combinatorial background. A small contribution from the $\Xi^0_b \to D^0 p K^-$ decay is observed and is included in the default $B^0_{(s)} \to \bar{D}^0 K^+ K^-$ fit, where its nonparametric PDF is obtained from simulation. The $\Lambda^0_b \to D^0 p \pi^-$ distribution is contaminated by the misidentified backgrounds $\Lambda^0_b \to D^0 p K^-$, $\Xi^0_b \to D^0 p K^-$, and $B^0_s \to \bar{D}^0 K^- \pi^+$ that partially extend outside the fitted region. These yields are corrected according to the expected fractions as computed from the simulation. The $\Lambda^0_b \to D^0 p K^-$, $\Xi^0_b \to D^0 p K^-$, and $\Lambda^0_b \to D^0 p \pi^-$ signals are modeled with Gaussian distributions, and since the $\Xi^0_b \to D^0 p K^-$ yield is small, the mass difference between the Λ^0_b and the Ξ^0_b baryons is fixed to its known value [39]. The effect of the latter constraint is minimal and is not associated with any systematic uncertainty. The combinatorial background is modeled with an exponential function, while other misidentified backgrounds are modeled by nonparametric PDFs obtained from simulation. As for the previous case with $B^0 \to \bar{D}^0 \pi^+ \pi^-$ candidates, alternative fits are applied, leading to consistent results where the largest variations are used to assign systematic uncertainties for the determination of the yields of the various components. A test is performed to include a specific cross-feed contribution from the channel $B^0_s \to \bar{D}^0 K^+ K^-$. No noticeable effect is observed, except on the yield of the $B^0_s \to \bar{D}^0 K^- \pi^+$ contribution. The outcome of this test is nevertheless included in the systematic uncertainty. The obtained yields for the $\Lambda^0_b \to D^0 p K^-$, $\Xi^0_b \to D^0 p \pi^-$, and $\Lambda^0_b \to D^0 p \pi^-$ decays are 193 ± 44, 64 ± 21, and 74 ± 32 events, respectively, where the systematic uncertainties are included. These yields and their uncertainties, listed in Table II, are used as Gaussian constraints in the fit to the $B^0_{(s)} \to \bar{D}^0 K^+ K^-$ invariant-mass distribution presented in Sec. V B.

V. INVARIANT-MASS FITS AND SIGNAL YIELDS

A. Likelihood function for the $B^0_{(s)} \to \bar{D}^0 h^+ h^-$ invariant-mass fit

The total probability density function $\mathcal{P}^{\text{tot}}_\theta(m_{\bar{D}^0 h^+ h^-})$ of the fitted parameters θ, is used in the extended likelihood function

$$\mathcal{L}_{\bar{D}^0 h^+ h^-} = \frac{v^n}{n!} e^{-v} \prod_{i=1}^{n} \mathcal{P}^{\text{tot}}_\theta(m_{i,\bar{D}^0 h^+ h^-}), \qquad (2)$$

where $m_{i,\bar{D}^0 h^+ h^-}$ is the invariant mass of candidate i, v is the sum of the yields and n the number of candidates observed in the sample. The likelihood function $\mathcal{L}_{\bar{D}^0 h^+ h^-}$ is maximized in the extended fit to the $m_{\bar{D}^0 h^+ h^-}$ invariant-mass distribution. The PDF for the $B^0 \to \bar{D}^0 \pi^+ \pi^-$ sample is

$$\mathcal{P}^{\text{tot}}_\theta(m_{\bar{D}^0 \pi^+ \pi^-}) = N_{\bar{D}^0 \pi^+ \pi^-} \times \mathcal{P}^{B^0}_{\text{sig}}(m_{\bar{D}^0 \pi^+ \pi^-})$$
$$+ \sum_{j=1}^{7} N_{j,\text{bkg}} \times \mathcal{P}_{j,\text{bkg}}(m_{\bar{D}^0 \pi^+ \pi^-}), \quad (3)$$

while that for $B^0_{(s)} \to \bar{D}^0 K^+ K^-$ decays is

$$\mathcal{P}^{\text{tot}}_\theta(m_{\bar{D}^0 K^+ K^-}) = N_{B^0 \to \bar{D}^0 K^+ K^-} \times \mathcal{P}^{B^0}_{\text{sig}}(m_{\bar{D}^0 K^+ K^-})$$
$$+ N_{B^0_s \to \bar{D}^0 K^+ K^-} \times \mathcal{P}^{B^0_s}_{\text{sig}}(m_{\bar{D}^0 K^+ K^-})$$
$$+ \sum_{j=1}^{9} N_{j,\text{bkg}} \times \mathcal{P}_{j,\text{bkg}}(m_{\bar{D}^0 K^+ K^-}). \qquad (4)$$

The PDFs used to model the signals $\mathcal{P}^{B^0_{(s)}}_{\text{sig}}(m_{\bar{D}^0 h^+ h^-})$ are defined by Eq. (1). The PDFs of each of the seven ($B^0 \to \bar{D}^0 \pi^+ \pi^-$) and nine ($B^0_{(s)} \to \bar{D}^0 K^+ K^-$) background components are presented in Sec. IV, while $N_{B^0_{(s)} \to \bar{D}^0 h^+ h^-}$ and $N_{j,\text{bkg}}$ are the signal and background yields, respectively.

B. Default fit and robustness tests

The default fit to the data is performed, using the MINUIT/MINOS [52] and the RooFit [53] software packages, in the mass-range $m_{\bar{D}^0 h^+ h^-} \in [5115, 6000]$ MeV/c^2. The fit results are given in Table III.

An unconstrained fit to the $m_{\bar{D}^0 \pi^+ \pi^-}$ distribution returns a negative $B^0_s \to \bar{D}^{*0} K^- \pi^+$ yield, which is consistent with zero within statistical uncertainties (-2167 ± 1514 events), while the expected yield is around 1.8% that of the signal yield, or 540 events (see Table I). The $B^0_s \to \bar{D}^{*0} K^- \pi^+$ contribution lies in the lower mass region, where background contributions are complicated, but have little effect on the signal yield determination. In the fit results listed in Table III, this contribution is fixed to be 540 events. The

TABLE III.   Parameters from the default fit to $B^0 \to \bar{D}^0\pi^+\pi^-$ and $B^0_{(s)} \to \bar{D}^0 K^+ K^-$ data samples in the invariant-mass range $m_{\bar{D}^0 h^+ h^-} \in [5115, 6000]$ MeV/c^2. The quantity χ^2/ndf corresponds to the reduced χ^2 of the fit for the corresponding number of degrees of freedom, ndf, while the p-value is the probability value associated with the fit and is computed with the method of least squares [39].

Parameter	$B^0 \to \bar{D}^0\pi^+\pi^-$	$B^0_{(s)} \to \bar{D}^0 K^+ K^-$
m_0 [MeV/c^2]	5282.0 ± 0.1	5282.6 ± 0.3
σ_1 [MeV/c^2]	9.7 ± 1.0	Fixed at 9.7
σ_2 [MeV/c^2]	16.2 ± 0.8	Fixed at 16.2
f_{CB}	0.3 ± 0.1	0.6 ± 0.1
a_{comb} [$10^{-3} \times$ (MeV/c^2)$^{-1}$]	-3.2 ± 0.1	-1.3 ± 0.4
$N_{B^0 \to \bar{D}^0 h^+ h^-}$	29943 ± 243	1918 ± 74
$N_{B^0_s \to \bar{D}^0 h^+ h^-}$	$\cdots$	473 ± 33
N_{comb}	20266 ± 463	1720 ± 231
$N_{B^0_s \to \bar{D}^0 K^- \pi^+}$	923 ± 191	151 ± 47
$N_{B^0 \to \bar{D}^0 K^+ \pi^-}$	2450 ± 211	131 ± 65
$N_{\Lambda^0_b \to D^0 p K^-}$ (constrained)	$\cdots$	197 ± 44
$N_{\Xi^0_b \to D^0 p K^-}$ (constrained)	$\cdots$	57 ± 20
$N_{\Lambda^0_b \to D^0 p \pi^-}$ (constrained)	1016 ± 136	74 ± 32
$N_{B^0_s \to \bar{D}^{*0} K^- \pi^+}$	540 (fixed)	833 ± 185
$N_{B^0_s \to \bar{D}^{*0} K^+ K^-}$	$\cdots$	775 ± 100
$N_{B^0 \to \bar{D}^{*0}[\bar{D}^0 \gamma]\pi^+\pi^-}$	7697 ± 325	$\cdots$
N_{Low-m}	14914 ± 222	1632 ± 68
χ^2/ndf (p-value)	52/46 (25%)	43/46 (60%)

difference in the signal yield with and without this constraint amounts to 77 events, which is included as a systematic uncertainty. The results obtained for the other backgrounds are consistent with the estimated relative yields computed in Sec. IV A. The fit uses Gaussian constraints in the fitted likelihood function for the yields of the modes $\Lambda^0_b \to D^0 p K^-$, $\Xi^0_b \to D^0 p \pi^-$, and $\Lambda^0_b \to D^0 p \pi^-$, as explained in Sec. IV E.

The fitted signal yields are $N_{B^0 \to \bar{D}^0 \pi^+\pi^-} = 29\,943 \pm 243$, $N_{B^0 \to \bar{D}^0 K^+ K^-} = 1918 \pm 74$, and $N_{B^0_s \to \bar{D}^0 K^+ K^-} = 473 \pm 33$ events respectively, and the ratio $r_{B^0_s/B^0} \equiv N_{B^0_s \to \bar{D}^0 K^+ K^-}/N_{B^0 \to \bar{D}^0 K^+ K^-}$ is $(24.7 \pm 1.7)\%$. The ratio $r_{B^0_s/B^0}$ is a parameter in the fit and is used in the computation of the ratio of branching fractions $\mathcal{B}(B^0_s \to \bar{D}^0 K^+ K^-)/\mathcal{B}(B^0 \to \bar{D}^0 K^+ K^-)$ [see Eq. (6)]. The $B^0_s \to \bar{D}^0 K^+ K^-$ signal is thus observed with an overwhelming statistical significance. The χ^2/ndf for each fit is very good. The data distributions and fit results are shown in Figs. 3–5 shows the same plots with logarithmic scale in order to visualize the shape and the magnitude of each of the various background components. The pull distributions, defined as $(n^{fit}_i - n_i)/\sigma^{fit}_i$ are also shown in Figs. 3 and 4, where the bin number i of the histogram of the $m_{\bar{D}^0 h^+ h^-}$ invariant mass contains n_i candidates and the fit function yields n^{fit}_i decays, with a
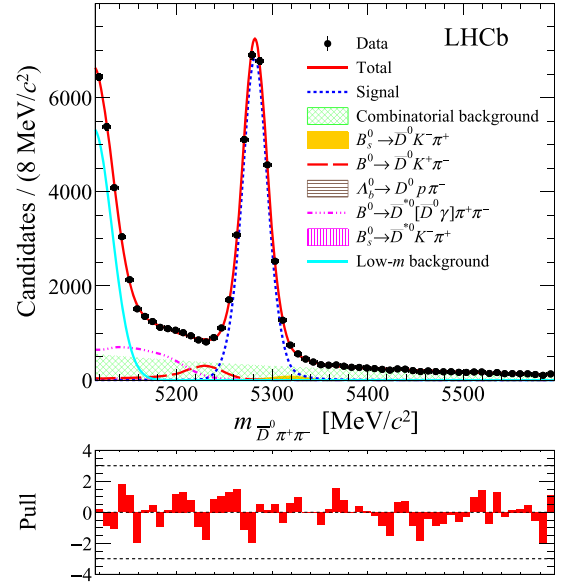
FIG. 3.   Fit to the $m_{\bar{D}^0 \pi^+ \pi^-}$ invariant-mass distribution with the associated pull plot.
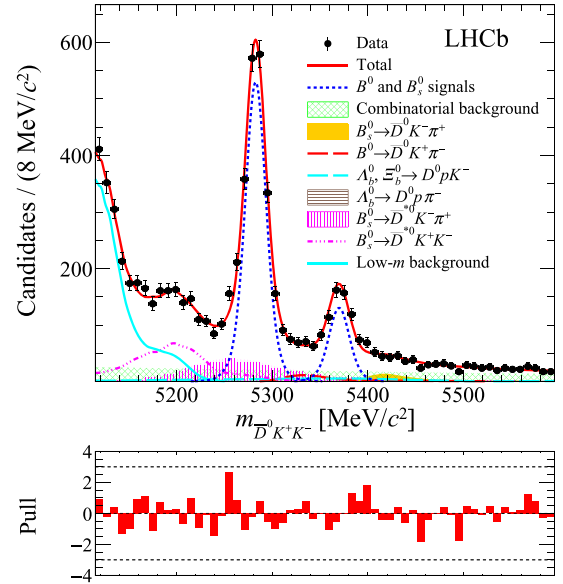
FIG. 4.   Fit to the $m_{\bar{D}^0 K^+ K^-}$ invariant-mass distribution with the associated pull plot.

statistical uncertainty σ^{fit}_i. The pull distributions show that the fits are unbiased.

For the $B^0_{(s)} \to D^0 K^+ K^-$ channels, the fitted contributions for the $B^0_s \to \bar{D}^0 K^- \pi^-$ and $B^0 \to \bar{D}^0 K^+ \pi^+$ decays are compatible with zero. These components are removed one by one in the default fit. The results of these tests are compatible with the output of the default fit. Therefore, no systematic uncertainty is applied.

Pseudoexperiments are generated using the default fit parameters with their uncertainties (see Table III), to build
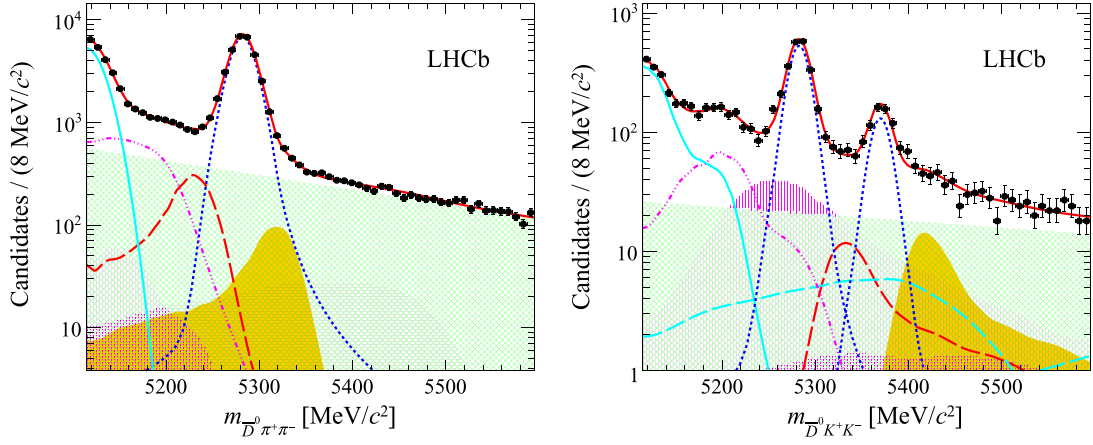
FIG. 5.   Fit to the (left) $m_{\bar{D}^0\pi^+\pi^-}$ invariant mass and (right) $m_{\bar{D}^0K^+K^-}$ invariant mass, in logarithmic vertical scale (see the legend on Figs. 3 and 4).

500 (1000) samples of $B^0 \to \bar{D}^0\pi^+\pi^-$ $(B^0_{(s)} \to \bar{D}^0K^+K^-)$ candidates according to the yields determined in data. The fit is then repeated on these samples to compute the three most important observables $N_{B^0\to\bar{D}^0\pi^+\pi^-}$, $N_{B^0\to\bar{D}^0K^+K^-}$, and $r_{B^0_s/B^0}$. No bias is seen in the three considered quantities. A coverage test is performed based on the associated pull distributions yields Gaussian distributions, with the expected mean and standard deviation. This test demonstrates that the statistical uncertainties on the yields obtained from the fit are well estimated.

VI. CALCULATION OF EFFICIENCIES AND BRANCHING FRACTION RATIOS

The ratios of branching fractions are calculated as

$$\frac{\mathcal{B}(B^0 \to \bar{D}^0K^+K^-)}{\mathcal{B}(B^0 \to \bar{D}^0\pi^+\pi^-)} = \frac{N_{B^0\to\bar{D}^0K^+K^-}}{N_{B^0\to\bar{D}^0\pi^+\pi^-}} \times \frac{\varepsilon_{B^0\to\bar{D}^0\pi^+\pi^-}}{\varepsilon_{B^0\to\bar{D}^0K^+K^-}} \quad (5)$$

and

$$\frac{\mathcal{B}(B^0_s \to \bar{D}^0K^+K^-)}{\mathcal{B}(B^0 \to \bar{D}^0K^+K^-)} = r_{B^0_s/B^0} \times \frac{\varepsilon_{B^0\to\bar{D}^0K^+K^-}}{\varepsilon_{B^0_s\to\bar{D}^0K^+K^-}} \times \frac{1}{f_s/f_d}, \quad (6)$$

where the yields are obtained from the fits described in Sec. V and the fragmentation factor ratio f_s/f_d is taken from Ref. [48]. The efficiencies ε account for effects related to reconstruction, triggering, PID and selection of the $B^0_{(s)} \to \bar{D}^0h^+h^-$ decays. These efficiencies vary over the Dalitz plot of the B decays. The total efficiency factorizes as

$$\varepsilon_{B^0_{(s)}\to\bar{D}^0h^+h^-} = \varepsilon^{\text{geom}} \times \varepsilon^{\text{sel|geom}} \times \varepsilon^{\text{PID|sel \& geom}}$$
$$\times \varepsilon^{\text{HW Trig|PID \& sel \& geom}}, \quad (7)$$

where $\varepsilon^{\text{X|Y}}$ is the efficiency of X relative to Y. The contribution $\varepsilon^{\text{geom}}$ is determined from the simulation,

and corresponds to the fraction of simulated decays which can be fully reconstructed within the LHCb detector acceptance. The term $\varepsilon^{\text{sel|geom}}$ accounts for the software part of the trigger system, the pre-filtering, the initial selection, the Fisher discriminant selection efficiencies, and for the effects related to the reconstruction of the charged tracks. It is computed with simulation, but the part related to the tracking includes corrections obtained from data control samples. The PID selection efficiency $\varepsilon^{\text{PID|sel \& geom}}$ is determined from the simulation corrected using pure and abundant $D^*(2010)^+ \to D^0\pi^+$ and $\Lambda \to p\pi^-$ calibration samples, selected using kinematic criteria only. Finally, $\varepsilon^{\text{HW Trig|PID \& sel \& geom}}$ is related to the effects due to the hardware part of the trigger system. Its computation is described in the next section.

As ratios of branching fractions are measured, only the ratios of efficiencies are of interest. Since the multiplicities of all the final states are the same, and the kinematic distributions of the decay products are similar, the uncertainties in the efficiencies largely cancel in the ratios of branching fractions. The main difference comes from the PID criteria for the $B^0 \to \bar{D}^0\pi^+\pi^-$ and $B^0 \to \bar{D}^0K^+K^-$ final states.

A. Trigger efficiency

The software trigger performance is well described in simulation and is included in $\varepsilon^{\text{sel|geom}}$. The efficiency of the hardware trigger depends on data-taking conditions and is determined from calibration data samples. The candidates are of type TOS or TIS, and both types (see Sec. II). the efficiency $\varepsilon^{\text{HW Trig|PID \& sel \& geom}}$ can be written as

$$\varepsilon^{\text{HW Trig|PID \& sel \& geom}} = \frac{N_{\text{TIS}} + N_{\text{TOS\&!TIS}}}{N_{\text{ref}}}$$
$$= \varepsilon^{\text{TIS}} + f \times \varepsilon^{\text{TOS}}, \quad (8)$$

where $\varepsilon^{\text{TIS}} = \frac{N_{\text{TIS}}}{N_{\text{ref}}}$, $f = \frac{N_{\text{TOS\&!TIS}}}{N_{\text{TOS}}}$, and $\varepsilon^{\text{TOS}} = \frac{N_{\text{TOS}}}{N_{\text{ref}}}$. The quantity N_{ref} is the number of signal decays that pass all the selection criteria, and $N_{\text{TOS\&!TIS}}$ is the number of candidates only triggered by TOS (i.e., not by TIS). Using Eq. (8), the hardware trigger efficiency is calculated from three observables: ε^{TIS}, f, and ε^{TOS}.

The quantities ε^{TIS} and f are effectively related to the TIS efficiency only. Therefore they are assumed to be the same for the three channels $B^0_{(s)} \to \bar{D}^0 h^+ h^-$ and are obtained from data. The value $f = (69 \pm 1)\%$ is computed using the number of signal candidates in the $B^0 \to \bar{D}^0 \pi^+ \pi^-$ sample obtained from a fit to data for each trigger requirement. The independence of this quantity with respect to the decay channel is checked both in simulation and in the data with the two $B^0_{(s)} \to \bar{D}^0 K^+ K^-$ modes. Similarly, the value of ε^{TIS} is found to be $(42.2 \pm 0.7)\%$.

The efficiency ε^{TOS} is computed for each of the three decay modes $B^0_{(s)} \to \bar{D}^0 h^+ h^-$ from phase-space simulated samples corrected with a calibration data set of $D^{*+} \to D^0 [K^- \pi^+] \pi^+$ decays. Studies of the trigger performance [54,55] provide a mapping for these corrections as a function of the type of the charged particle (kaon or pion), its electric charge, p_{T}, the region of the calorimeter region it impacts, the magnet polarity (up or down), and the time period of data taking (year 2011 or 2012). The value of ε^{TOS} for each of the three signals is listed in Table IV.

B. Total efficiency

The simulated samples used to obtain the total selection efficiency $\varepsilon_{B^0_{(s)} \to \bar{D}^0 h^+ h^-}$ are generated with phase-space models for the three-body $B^0_{(s)} \to \bar{D}^0 h^+ h^-$ decays. The three-body distributions in data are, however, significantly nonuniform (see Sec. VIII). Therefore corrections on $\varepsilon_{B^0_{(s)} \to \bar{D}^0 h^+ h^-}$ are derived to account for the Dalitz plot structures in the considered decays. The relative selection efficiency as a function of the $\bar{D}^0 h^+$ and the $\bar{D}^0 h^-$ squared invariant masses, $\varepsilon(m^2_{\bar{D}^0 h^+}, m^2_{\bar{D}^0 h^-})$, is determined from simulation and parametrized with a polynomial function of fourth order. The function $\varepsilon(m^2_{\bar{D}^0 h^+}, m^2_{\bar{D}^0 h^-})$ is normalized such that its integral is unity over the kinematically allowed phase space. The total efficiency correction $\bar{\varepsilon}^{\text{DP}}_{\text{corr}}$ factor is calculated, accounting for the position of each candidate across the Dalitz plot, as

$$\bar{\varepsilon}^{\text{DP}}_{\text{corr}} = \frac{\sum_i \omega_i}{\sum_i \omega_i / \varepsilon(m^2_{i,\bar{D}^0 h^+}, m^2_{i,\bar{D}^0 h^-})}, \quad (9)$$

where $m^2_{i,\bar{D}^0 h^+}$ and $m^2_{i,\bar{D}^0 h^-}$ are the squared invariant masses of the $\bar{D}^0 h^+$ and $\bar{D}^0 h^-$ combinations for the ith candidate in data, and ω_i is its signal $sWeight$ obtained from the default fit to the $B^0_{(s)} \to \bar{D}^0 h^+ h^-$ invariant-mass distribution

TABLE IV. Total efficiencies $\varepsilon_{B^0_{(s)} \to \bar{D}^0 h^+ h^-}$ and their contributions (before and after accounting for three-body decay kinematic properties) for the each three modes $B^0 \to \bar{D}^0 \pi^+ \pi^-$, $B^0 \to \bar{D}^0 K^+ K^-$, and $B^0_s \to \bar{D}^0 K^+ K^-$. Uncertainties are statistical only and those smaller than 0.1 are displayed as 0.1, but are accounted with their nominal values in the efficiency calculations.

	$B^0 \to \bar{D}^0 \pi^+ \pi^-$	$B^0 \to \bar{D}^0 K^+ K^-$	$B^0_s \to \bar{D}^0 K^+ K^-$
$\varepsilon^{\text{geom}}$ [%]	15.8 ± 0.1	17.0 ± 0.1	16.9 ± 0.1
$\varepsilon^{\text{sel\|geom}}$ [%]	1.2 ± 0.1	1.1 ± 0.1	1.1 ± 0.1
$\varepsilon^{\text{PID\|sel \& geom}}$ [%]	95.5 ± 1.2	75.7 ± 1.4	76.3 ± 2.0
ε^{TIS} [%]	42.2 ± 0.7	42.2 ± 0.7	42.2 ± 0.7
ε^{TOS} [%]	40.6 ± 0.6	40.3 ± 0.8	40.6 ± 1.2
$\bar{\varepsilon}^{\text{DP}}_{\text{corr}}$ [%]	85.5 ± 2.9	95.7 ± 4.1	$101.0^{+3.2}_{-7.1}$
$\varepsilon^{\text{TIS}}_{B^0_{(s)} \to \bar{D}^0 h^+ h^-}$ $[10^{-4}]$	6.4 ± 0.2	5.9 ± 0.3	$6.0^{+0.3}_{-0.5}$
$\varepsilon^{\text{TOS}}_{B^0_{(s)} \to \bar{D}^0 h^+ h^-}$ $[10^{-4}]$	6.1 ± 0.2	5.7 ± 0.3	$5.8^{+0.3}_{-0.5}$
$\varepsilon_{B^0_{(s)} \to \bar{D}^0 h^+ h^-}$ $[10^{-4}]$	10.6 ± 0.3	9.8 ± 0.4	$10.1^{+0.4}_{-0.6}$

$(m_{B^0_{(s)}} \in [5115, 6000]\ \text{MeV}/c^2)$. The statistical uncertainties on the efficiency corrections is evaluated with 1000 pseudoexperiments for each decay mode. The computation of the average efficiency is validated with an alternative procedure in which the phase space is divided into 100 bins for the $B^0 \to \bar{D}^0 \pi^+ \pi^-$ normalization channel and 20 bins for the $B^0_{(s)} \to \bar{D}^0 K^+ K^-$ signal modes. This binning is obtained according to the efficiency map of each decay, where areas with similar efficiencies are grouped together. The total average efficiency is then computed as a function of the efficiency and the number of candidates in each bin. The two methods give compatible results within the uncertainties. The values of $\bar{\varepsilon}^{\text{DP}}_{\text{corr}}$ for each of the three signals are listed in Table IV.

Table IV shows the value of the total efficiency $\varepsilon_{B^0_{(s)} \to \bar{D}^0 h^+ h^-}$ and its contributions. The relative values of $\varepsilon^{\text{TIS}}_{B^0_{(s)} \to \bar{D}^0 h^+ h^-}$ and $\varepsilon^{\text{TOS}}_{B^0_{(s)} \to \bar{D}^0 h^+ h^-}$, for TIS and TOS triggered candidates, are also given. The total efficiency is obtained as [see Eq. (8)]

$$\varepsilon_{B^0_{(s)} \to \bar{D}^0 h^+ h^-} = \varepsilon^{\text{TIS}}_{B^0_{(s)} \to \bar{D}^0 h^+ h^-} + f \times \varepsilon^{\text{TOS}}_{B^0_{(s)} \to \bar{D}^0 h^+ h^-}, \quad (10)$$

where $f = (69 \pm 1)\%$. The total efficiencies for the three $B^0_{(s)} \to \bar{D}^0 h^+ h^-$ modes are compatible within their uncertainties.

VII. SYSTEMATIC UNCERTAINTIES

Many sources of systematic uncertainty cancel in the ratios of branching fractions. Other sources are described below.

A. Trigger

The calculation of the hardware trigger efficiency is described in Sec. VI A. To determine $\varepsilon^{\text{HW Trig|PID \& sel \& geom}}$, a data-driven method is exploited. It is based on ε^{TOS}, as described in Refs. [55,56], and on the quantities f and ε^{TIS}, determined on the data normalization channel $B^0 \to \bar{D}^0 \pi^+ \pi^-$ [see Eq. (8)]. The latter two quantities depend on the TIS efficiency of the hardware trigger and are assumed to be the same for all three modes. The values of f and ε^{TIS} are consistent for the $B^0 \to \bar{D}^0 K^+ K^-$ and the $B_s^0 \to \bar{D}^0 K^+ K^-$ channels; no systematic uncertainty is assigned for this assumption. Simulation studies show that these values are consistent for $B^0 \to \bar{D}^0 K^+ K^-$ and $B^0 \to \bar{D}^0 \pi^+ \pi^-$ channels. A 2.0% systematic uncertainty, corresponding to the maximum observed deviation with simulation, is assigned on the ratio of their relative $\varepsilon^{\text{HW Trig|PID \& sel \& geom}}$ efficiencies.

B. PID

A systematic uncertainty is associated with the efficiency $\varepsilon^{\text{PID|sel \& geom}}$ when final states of the signal and normalization channels are different. For each track which differs in the signal channel $B^0 \to \bar{D}^0 K^+ K^-$ and the normalization channel $B^0 \to \bar{D}^0 \pi^+ \pi^-$, an uncertainty of 0.5% per track due to the kaon or pion identification requirement is applied (e.g., see Refs. [19,57]). As the same PID requirements are used for $\bar{D}^0$ decay products for all modes, the charged tracks from those decay products do not need to be considered. The relevant systematic uncertainties are added linearly to account for correlations in these uncertainties. An overall PID systematic uncertainty of 2.0% on the ratio $\mathcal{B}(B^0 \to \bar{D}^0 K^+ K^-)/\mathcal{B}(B^0 \to \bar{D}^0 \pi^+ \pi^-)$ is assigned.

C. Signal and background modeling

Systematic effects due to the imperfect modeling of both the signal and background distributions in the fit to $m_{\bar{D}^0 h^+ h^-}$ are studied. Additional components are considered for each fit on $m_{\bar{D}^0 \pi^+ \pi^-}$ and $m_{\bar{D}^0 K^+ K^-}$. Moreover the impact of backgrounds with a negative yield, or compatible with zero at one standard deviation is evaluated. The various sources of systematic uncertainties discussed in this section are given in Table V. The main sources are related to resolution effects and to the modeling of the signal and background PDFs.

A systematic uncertainty is assigned for the modeling of the PDF $\mathcal{P}_{\text{sig}}$, defined in Eq. (1). The value of the tail parameters $\alpha_{1,2}$ and $n_{1,2}$ are fixed to those obtained from simulation. To test the validity of this constraint, new sets of tail parameters, compatible with the covariance matrix obtained from a fit to simulated signal decays, are generated and used as new fixed values. The variance of the new fitted yields is 1.0% of the yield $N_{B^0 \to \bar{D}^0 \pi^+ \pi^-}$, which is taken as the associated systematic uncertainty. For the fit to

TABLE V. Relative systematic uncertainties, in percent, on $N_{B^0 \to \bar{D}^0 \pi^+ \pi^-}$, $N_{B^0 \to \bar{D}^0 K^+ K^-}$ and the ratio $N_{B^0 \to \bar{D}^0 \pi^+ \pi^-}/N_{B^0 \to \bar{D}^0 K^+ K^-}$ and $r_{B_s^0/B^0}$, due to PDFs modeling in the $m_{\bar{D}^0 \pi^+ \pi^-}$ and $m_{\bar{D}^0 K^+ K^-}$ fits. The uncertainties are uncorrelated and summed in quadrature.

Source	$N_{B^0 \to \bar{D}^0 \pi^+ \pi^-}$	$N_{B^0 \to \bar{D}^0 K^+ K^-}$	$r_{B_s^0/B^0}$
$B_{(s)}^0 \to \bar{D}^0 h^+ h^-$ signal PDF	1.0	2.1	4.2
$B^0 \to \bar{D}^{*0}[\bar{D}^0 \gamma] \pi^+ \pi^-$	1.6	⋯	⋯
$B^0 \to \bar{D}^0 K^+ \pi^-$	0.3	⋯	⋯
$B_s^0 \to \bar{D}^{*0} K^- \pi^+$	0.4	1.4	0.4
$B_s^0 \to \bar{D}^{*0} K^+ K^-$	⋯	0.5	1.3
Smearing and shifting	0.5	0.1	0.9
Total	2.0	2.6	4.5
Total on $N_{\text{sig}}/N_{\text{normal}}$		3.2	4.5

the $B_{(s)}^0 \to \bar{D}^0 K^+ K^-$ candidates, the above changes to the tail parameters correspond to a 1.4% relative effect on the yield $N_{B^0 \to \bar{D}^0 K^+ K^-}$ and 0.4% on the ratio $r_{B_s^0/B^0}$. Another systematic uncertainty is linked to the relative resolution of the $B_s^0 \to \bar{D}^0 K^+ K^-$ mass peak with respect to that of the $B^0 \to \bar{D}^0 K^+ K^-$ signal. In the default fit, the resolutions of these two modes are fixed to be the same. Alternatively, the relative difference of the resolution for the two modes can be taken to be proportional to the kinetic energy released in the decay, $Q_{d,(s)} = m_{B_{(s)}^0} - m_{\bar{D}^0} - 2m_X$, where m_X indicates the known mass of the X meson, so that the resolution of the B^0 signal stays unchanged, while that of the B_s^0 distribution is multiplied by $Q_s/Q_d = 1.02$. The latter effect results in a small change of 0.2% on $N_{B^0 \to \bar{D}^0 K^+ K^-}$, as expected, and a larger variation of 1.7% on $r_{B_s^0/B^0}$. A third systematic uncertainty on $B_{(s)}^0 \to \bar{D}^0 K^+ K^-$ signal modeling is computed to account for the mass difference Δm_B which is fixed in this fit (see Sec. IV B). When left free in the fit, the measured mass difference $\Delta m_B = 88.29 \pm 1.23$ MeV/c^2 is consistent with the value fixed in the default fit, which creates a relative change of 1.6% on $N_{B^0 \to \bar{D}^0 K^+ K^-}$ and a larger one of 3.8% on $r_{B_s^0/B^0}$. These three sources of systematic uncertainty on the $B_{(s)}^0 \to \bar{D}^0 K^+ K^-$ invariant-mass modeling are considered as uncorrelated, and are added in quadrature to obtain a global relative systematic uncertainty of 2.1% on the yield $N_{B^0 \to \bar{D}^0 K^+ K^-}$ and 4.2% on the ratio $r_{B_s^0/B^0}$.

For the default fit on $m_{\bar{D}^0 \pi^+ \pi^-}$ (see Table III), the $B^0 \to \bar{D}^{*0}[\bar{D}^0 \gamma] \pi^+ \pi^-$ and $B^0 \to \bar{D}^0 K^+ \pi^-$ components are the main peaking backgrounds and the contribution from $B_s^0 \to \bar{D}^{*0} K^- \pi^+$ is fixed to the expected value from simulation. The $B^0 \to \bar{D}^{*0}[\bar{D}^0 \gamma] \pi^+ \pi^-$ background is modeled in the default fit with a nonparametric PDF determined on a phase-space simulated sample of $B^0 \to \bar{D}^{*0}[\bar{D}^0 \gamma] \pi^+ \pi^-$ decays. In an alternative approach, the modeling of that background is replaced by nonparametric PDFs determined

from simulated samples of $B^0 \to \bar{D}^{*0}[\bar{D}^0\gamma]\rho^0$ decays with various polarizations. Two values for the longitudinal polarization fraction are tried, one from the color-suppressed mode $B^0 \to \bar{D}^{*0}\omega$, $f_L = (66.5 \pm 4.7 \pm 1.5)\%$ [58] (this result is consistent with the result presented in Ref. [59]) and the other from the color-allowed mode $B^0 \to D^{*-}\rho^+$, $f_L = (88.5 \pm 1.6 \pm 1.2)\%$ [60]. A systematic uncertainty of 1.6% for the $B^0 \to \bar{D}^{*0}[\bar{D}^0\gamma]\pi^+\pi^-$ modeling, corresponding to the largest deviation from the nominal result, is assigned. A different model of simulation for the generation of the background $B^0 \to \bar{D}^0 K^+\pi^-$ decays is used to define the nonparametric PDF used in the invariant-mass fit. The first is a phase-space model where the generated signals decays are uniformly distributed over a regular-Dalitz plot, while the other is uniformly distributed over the square version of the Dalitz plot. The definition of the square-Dalitz plots is given in Ref. [21]. The difference between these two PDFs for the $B^0 \to \bar{D}^0 K^+\pi^-$ background corresponds to a 0.3% relative effect. The component $B^0_s \to \bar{D}^{*0}K^-\pi^+$ is found to be initially negative (and compatible with zero) and then fixed in the default fit, resulting in a relative systematic uncertainty of 0.4%.

The main background channels in the fit to $m_{\bar{D}^0 K^+ K^-}$ are $B^0_s \to \bar{D}^{*0}K^+K^-$ and $B^0_s \to \bar{D}^{*0}K^-\pi^+$. The nonparametric PDF for $B^0_s \to \bar{D}^{*0}K^+K^-$ decays is computed from an alternative simulated sample, where the nominal phase-space simulation is replaced by that computed with a square-Dalitz plot generation of the simulated decays. The measured difference between the two models results in relative systematic uncertainties on $N_{B^0 \to \bar{D}^0 K^+ K^-}$ and $r_{B^0_s/B^0}$ of 0.5% and 1.3%, respectively. The component $B^0_s \to \bar{D}^{*0}K^-\pi^+$ is modeled with a nonparametric PDF from the square-Dalitz plot simulation. Alternatively, the PDF of the $B^0_s \to \bar{D}^{*0}K^-\pi^+$ background is modeled with a nonparametric PDF determined from a simulated sample of $B^0_s \to \bar{D}^{*0}\bar{K}^{*0}$ decays, with polarization taken from the similar mode $B^+ \to \bar{D}^{*0}K^{*+}$, $f_L = (86 \pm 6 \pm 3)\%$ [61]. The difference obtained for these two PDF models for the $B^0_s \to \bar{D}^{*0}K^-\pi^+$ background gives relative systematic uncertainties on $N_{B^0 \to \bar{D}^0 K^+ K^-}$ and r_{B_s/B_d} equal to 1.4% and 0.4%.

Systematic uncertainties for the constrained $\Lambda^0_b \to D^0 pK^-$ or $\Lambda^0_b \to D^0 p\pi^-$ and $\Xi^0_b \to D^0 p\pi^-$ decay yields are discussed in Sec. IV E and are already taken into account when fitting the $B^0_{(s)} \to \bar{D}^0 h^+ h^-$ invariant-mass distributions.

Finally, the impact of the simulation tuning that is described in Sec. IV D is evaluated by performing the default fit without modifying the PDFs of the various backgrounds to match the width and mean invariant masses seen in data. The resulting discrepancies give a relative effect of 0.5% on $N(B^0 \to \bar{D}^0\pi^+\pi^-)$, 0.1% on $N(B^0 \to \bar{D}^0 K^+ K^-)$, and 0.9% on $r_{B^0_s/B^0}$.

TABLE VI.   Relative systematic uncertainties, in percent, on the ratio of branching fractions $\mathcal{R}_{\bar{D}^0 K^+ K^-/\bar{D}^0\pi^+\pi^-}$ and $\mathcal{R}_{B^0_s/B^0}$. The uncertainties are uncorrelated and summed in quadrature.

Source	$\mathcal{R}_{\bar{D}^0 K^+ K^-/\bar{D}^0\pi^+\pi^-}$	$\mathcal{R}_{B^0_s/B^0}$
HW trigger efficiency	2.0	$\cdots$
PID efficiency	2.0	$\cdots$
PDF modeling	3.2	4.5
f_s/f_d	$\cdots$	5.8
Total	4.3	7.3

D. Summary of systematic uncertainties

The systematic uncertainties contributing to the ratio of branching fractions $\mathcal{R}_{\bar{D}^0 K^+ K^-/\bar{D}^0\pi^+\pi^-} \equiv \mathcal{B}(B^0 \to \bar{D}^0 K^+ K^-)/\mathcal{B}(B^0 \to \bar{D}^0\pi^+\pi^-)$ [see Eq. (5)] and for the ratio $\mathcal{R}_{B^0_s/B^0} \equiv \mathcal{B}(B^0_s \to \bar{D}^0 K^+ K^-)/\mathcal{B}(B^0 \to \bar{D}^0 K^+ K^-)$ [see Eq. (6)] are listed in Table VI. All sources of systematic uncertainties are uncorrelated and are therefore summed in quadrature. For the ratio $\mathcal{R}_{B^0_s/B^0}$ the external input $f_s/f_d = 0.259 \pm 0.015$ [48] introduces the dominant systematic uncertainty of 5.8%.

VIII. RESULTS

The ratios of branching fractions are measured to be

$$\frac{\mathcal{B}(B^0 \to \bar{D}^0 K^+ K^-)}{\mathcal{B}(B^0 \to \bar{D}^0\pi^+\pi^-)} = (6.9 \pm 0.4 \pm 0.3)\% \quad (11)$$

and

$$\frac{\mathcal{B}(B^0_s \to \bar{D}^0 K^+ K^-)}{\mathcal{B}(B^0 \to \bar{D}^0 K^+ K^-)} = (93.0 \pm 8.9 \pm 6.9)\%, \quad (12)$$

where the first uncertainties are statistical and the second are systematic. Using the branching fraction $\mathcal{B}(B^0 \to \bar{D}^0\pi^+\pi^-) = (8.8 \pm 0.5) \times 10^{-4}$ [39], the branching fraction of the $B^0 \to \bar{D}^0 K^+ K^-$ decay is measured to be

$$\mathcal{B}(B^0 \to \bar{D}^0 K^+ K^-) = (6.1 \pm 0.4 \pm 0.3 \pm 0.3) \times 10^{-5}, \quad (13)$$

where the third uncertainty is due to the limited knowledge of $\mathcal{B}(B^0 \to \bar{D}^0\pi^+\pi^-)$. The branching ratio of the decay $B^0_s \to \bar{D}^0 K^+ K^-$ is measured to be

$$\mathcal{B}(B^0_s \to \bar{D}^0 K^+ K^-) = (5.7 \pm 0.5 \pm 0.4 \pm 0.5) \times 10^{-5}, \quad (14)$$

where the third uncertainty is due to the limited knowledge of $\mathcal{B}(B^0 \to \bar{D}^0 K^+ K^-)$. These results are compatible with and more precise than the previous LHCb results [18] for the same decays, i.e., $\mathcal{B}(B^0 \to \bar{D}^0 K^+ K^-) = (4.7 \pm 0.9 \pm 0.6 \pm 0.5) \times 10^{-5}$ and $\mathcal{B}(B^0_s \to \bar{D}^0 K^+ K^-) = (4.2 \pm 1.3 \pm 0.9 \pm 1.1) \times 10^{-5}$, which were based on a
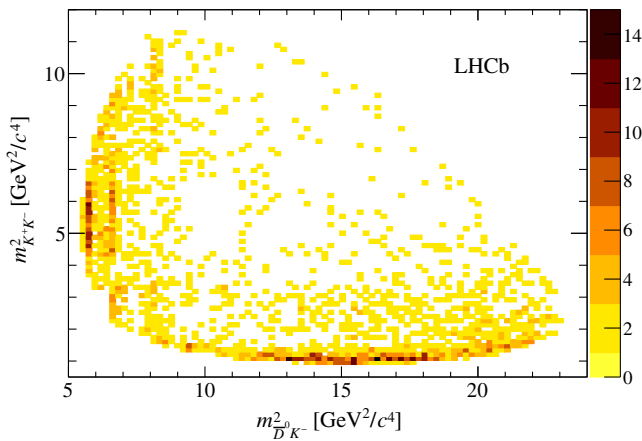
FIG. 6. Dalitz plot for $B^0 \to \bar{D}^0 K^+ K^-$ candidates in the signal region $m_{\bar{D}^0 K^+ K^-} \in [5240, 5320]$ MeV/c^2.
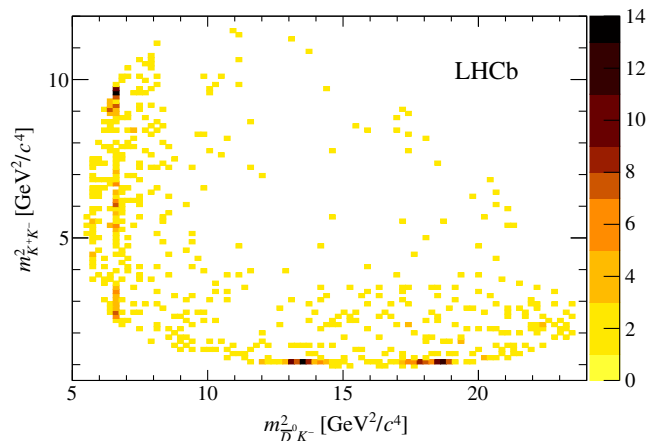

FIG. 7. Dalitz plot for $B_s^0 \to \bar{D}^0 K^+ K^-$ candidates in the signal region $m_{\bar{D}^0 K^+ K^-} \in [5327, 5407]$ MeV/c^2.

subset of the current data set. The measurement of the branching ratios $\mathcal{B}(B_{(s)}^0 \to \bar{D}^0 K^+ K^-)$ is the first step towards a Dalitz plot analysis of these modes using the LHC Run-2 data sample. Nonetheless, an inspection of the Dalitz plot is performed and several structures are visible in the $B^0 \to \bar{D}^0 K^+ K^-$ and $B_s^0 \to \bar{D}^0 K^+ K^-$ decays.

The Dalitz plot ($m_{\bar{D}^0 K^-}^2$, $m_{K^- K^+}^2$) distribution of $B^0 \to \bar{D}^0 K^+ K^-$ candidates populating the B^0 signal mass range, $m_{\bar{D}^0 K^+ K^-} \in [5240, 5320]$ MeV/c^2 (i.e., ± 40 MeV/c^2 around the B^0 mass) is displayed in Fig. 6. Several resonances are clearly visible. In the $K^+ K^-$ system, some unknown combination of the resonances $a_0(980)$ and $f_0(980)$ seem to be dominant. The search for the rare $B^0 \to \bar{D}^0 \phi$ decay using the same data sample is described in a separate publication [22]. For the $\bar{D}^0 K^-$ system, the first band below 6 GeV^2/c^4 corresponds to the partially reconstructed decay $B_s^0 \to D_{s1}(2536)^- K^+/\pi^+$, with $D_{s1}(2536)^- \to \bar{D}^{*0} K^-$ (i.e., a background component due to the decay $B_s^0 \to \bar{D}^{*0} K^- K^+$ or $B_s^0 \to \bar{D}^{*0} K^- \pi^+$, with the pion misidentified). The decay $D_{s1}(2536)^- \to \bar{D}^0 K^-$ is forbidden by the conservation of parity in strong interactions and cannot explain the observed feature. The second band around 6.6 GeV^2/c^4 is related to the mode $B^0 \to D_{s2}^*(2573)^- K^+$, with $D_{s2}^*(2573)^- \to \bar{D}^0 K^-$ and a third vertical band can be distinguished at about 8.2 GeV^2/c^4 which corresponds to a potential superposition of the $D_{s1}^*(2860)^-$ and the $D_{s3}^*(2860)^-$ resonances previously observed by LHCb [23,62].

The Dalitz plot ($m_{\bar{D}^0 K^-}^2$, $m_{K^- K^+}^2$) distribution of $B_{(s)}^0 \to \bar{D}^0 K^+ K^-$ candidates populating the B_s^0 signal mass range, $m_{\bar{D}^0 K^+ K^-} \in [5327, 5407]$ MeV/c^2 (i.e., ± 40 MeV/c^2 around the B_s^0 mass) is shown in Fig. 7. Again, several resonances can be clearly identified. In the $K^+ K^-$ system, the ϕ resonance is observed and the study of the corresponding decay is presented in a separate publication [22].

There is some possible accumulation of candidates in a broad structure around 1.7 GeV/c^2, which may correspond to the $\phi(1680)$ state. In addition, in the $\bar{D}^0 K^-$ system, the $D_{s2}^*(2573)^-$ resonance is identifiable.

An analysis with additional LHCb data will enable the study of D_s^{**} spectroscopy, particularly those resonances that are natural spin-parity members of the $1D$ and $1F$ families. The differences between the B^0 and B_s^0 modes are also interesting. In addition, different resonances can contribute strongly with respect to $B_s^0 \to \bar{D}^0 K^- \pi^+$ decays [23,62].

---

[1] N. Cabibbo, Unitary Symmetry and Leptonic Decays, Phys. Rev. Lett. **10,** 531 (1963).

[2] M. Kobayashi and T. Maskawa, *CP*-violation in the renormalizable theory of weak interaction, Prog. Theor. Phys. **49,** 652 (1973).

[3] J. Brod and J. Zupan, The ultimate theoretical error on γ from $B \to DK$ decays, J. High Energy Phys. 01 (2014) 051.

[4] J. Brod, A. Lenz, G. Tetlalmatzi-Xolocotzi, and M. Wiebusch, New physics effects in tree-level decays and the precision in the determination of the quark mixing angle γ, Phys. Rev. D **92,** 033002 (2015).

[5] J. Charles, S. Descotes-Genon, Z. Ligeti, S. Monteil, M. Papucci, and K. Trabelsi, Future sensitivity to new physics in B_d, B_s, and K mixings, Phys. Rev. D **89,** 033016 (2014).

[6] A. J. Bevan *et al.* (Belle and *BABAR* Collaborations), The physics of the B factories, Eur. Phys. J. C **74,** 3026 (2014).

[7] Y. Amhis *et al.* (Heavy Flavor Averaging Group), Averages of b-hadron, c-hadron, and τ-lepton properties as of summer 2016, Eur. Phys. J. C **77,** 895 (2017); updated results and plots available at https://hflav.web.cern.ch.

[8] R. Aaij *et al.* (LHCb Collaboration), Measurement of the CKM angle γ from a combination of LHCb results, J. High Energy Phys. 12 (2016) 087.

[9] LHCb Collaboration, Update of the LHCb combination of the CKM angle γ, CERN Report No. LHCb-CONF-2018-002, (2018).

[10] R. Aaij *et al.* (LHCb Collaboration), Measurement of *CP* asymmetry in $B_s^0 \to D_s^{\mp} K^{\pm}$ decays, J. High Energy Phys. 03 (2018) 059.

[11] R. Aaij *et al.* (LHCb Collaboration), Measurement of the CKM angle γ using $B^{\pm} \to DK^{\pm}$ with $D \to K_S^0 \pi^+ \pi^-$, $K_S^0 K^+ K^-$ decays, J. High Energy Phys. 08 (2018) 176.

[12] M. Gronau and D. London, How to determine all the angles of the unitarity triangle from $B^0 \to DK_S^0$ and $B_s^0 \to D\phi$, Phys. Lett. B **253,** 483 (1991).

[13] M. Gronau, Y. Grossman, N. Shuhmaher, A. Soffer, and J. Zupan, Using untagged $B^0 \to DK_S^0$ to determine γ, Phys. Rev. D **69,** 113003 (2004).

[14] M. Gronau, Y. Grossman, Z. Surujon, and J. Zupan, Enhanced effects on extracting γ from untagged B^0 and B_s^0 decays, Phys. Lett. B **649,** 61 (2007).

[15] S. Ricciardi, Measuring the CKM angle γ at LHCb using untagged $B_s \to D\phi$ decays, CERN Report No. LHCb-PUB-2010-005, (2010).

[16] S. Nandi and D. London, $B_s(\bar{B}_s) \to D_{CP}^0 K\bar{K}$: Detecting and discriminating new physics in $B_s - \bar{B}_s$ mixing, Phys. Rev. D **85,** 114015 (2012).

[17] R. Aaij *et al.* (LHCb Collaboration), Observation of the decay $B_s^0 \to \bar{D}^0 \phi$, Phys. Lett. B **727,** 403 (2013).

[18] R. Aaij *et al.* (LHCb Collaboration), Observation of $B^0 \to \bar{D}^0 K^+ K^-$ and Evidence for $B_s^0 \to \bar{D}^0 K^+ K^-$, Phys. Rev. Lett. **109,** 131801 (2012).

[19] R. Aaij *et al.* (LHCb Collaboration), Measurements of the branching fractions of the decays $B_s^0 \to \bar{D}^0 K^- \pi^+$ and $B^0 \to \bar{D}^0 K^+ \pi^-$, Phys. Rev. D **87,** 112009 (2013).

[20] R. Aaij *et al.* (LHCb Collaboration), Study of beauty baryon decays to $D^0 ph^-$ and $\Lambda_c^+ h^-$ final states, Phys. Rev. D **89,** 032001 (2014).

[21] R. Aaij *et al.* (LHCb Collaboration), Dalitz plot analysis of $B^0 \to \bar{D}^0 \pi^+ \pi^-$ decays, Phys. Rev. D **92,** 032002 (2015).

[22] R. Aaij *et al.* (LHCb Collaboration), Observation of $B_s^0 \to \bar{D}^{*0} \phi$ and search for $B^0 \to \bar{D}^0 \phi$ decays, arXiv:1807.01892.

[23] R. Aaij *et al.* (LHCb Collaboration), Dalitz plot analysis of $B_s^0 \to \bar{D}^0 K^- \pi^+$ decays, Phys. Rev. D **90,** 072003 (2014).

[24] A. A. Alves, Jr. *et al.* (LHCb Collaboration), The LHCb detector at the LHC, J. Instrum. **3,** S08005 (2008).

[25] R. Aaij *et al.* (LHCb Collaboration), LHCb detector performance, Int. J. Mod. Phys. A **30,** 1530022 (2015).

[26] R. Aaij *et al.*, Performance of the LHCb vertex locator, J. Instrum. **9,** P09007 (2014).

[27] R. Arink *et al.*, Performance of the LHCb outer tracker, J. Instrum. **9,** P01002 (2014).

[28] M. Adinolfi *et al.*, Performance of the LHCb RICH detector at the LHC, Eur. Phys. J. C **73,** 2431 (2013).

[29] A. A. Alves, Jr. *et al.*, Performance of the LHCb muon system, J. Instrum. **8,** P02022 (2013).

[30] V. V. Gligorov and M. Williams, Efficient, reliable and fast high-level triggering using a bonsai boosted decision tree, J. Instrum. **8,** P02013 (2013).

[31] A. Kuzmin *et al.* (Belle Collaboration), Study of $\bar{B}^0 \to D^0 \pi^+ \pi^-$ decays, Phys. Rev. D **76,** 012006 (2007).

[32] T. Sjöstrand, S. Mrenna, and P. Skands, A brief introduction to PYTHIA 8.1, Comput. Phys. Commun. **178,** 852 (2008).

[33] I. Belyaev *et al.*, Handling of the generation of primary events in Gauss, the LHCb simulation framework, J. Phys. Conf. Ser. **331,** 032047 (2011).

[34] D. J. Lange, The EvtGen particle decay simulation package, Nucl. Instrum. Methods Phys. Res., Sect. A **462,** 152 (2001).

[35] P. Golonka and Z. Was, PHOTOS Monte Carlo: A precision tool for QED corrections in Z and W decays, Eur. Phys. J. C **45,** 97 (2006).

[36] J. Allison *et al.* (Geant4 Collaboration), Geant4 developments and applications, IEEE Trans. Nucl. Sci. **53,** 270 (2006); S. Agostinelli *et al.* (Geant4 Collaboration), Geant4: A simulation toolkit, Nucl. Instrum. Methods Phys. Res., Sect. A **506,** 250 (2003).

[37] M. Clemencic, G. Corti, S. Easo, C. R. Jones, S. Miglioranzi, M. Pappagallo, and P. Robbe, The LHCb simulation application, Gauss: Design, evolution and experience, J. Phys. Conf. Ser. **331**, 032023 (2011).

[38] R. Aaij et al. (LHCb Collaboration), Search for the decay $B_s^0 \to D_s^{*\mp}\pi^\pm$, Phys. Rev. D **87**, 071101(R) (2013).

[39] M. Tanabashi et al. (Particle Data Group), Review of particle physics, Phys. Rev. D **98**, 030001 (2018).

[40] W. D. Hulsbergen, Decay chain fitting with a Kalman filter, Nucl. Instrum. Methods Phys. Res., Sect. A **552**, 566 (2005).

[41] H. Voss, A. Hoecker, J. Stelzer, and F. Tegenfeldt, TMVA—Toolkit for multivariate data analysis, Proc. Sci. ACAT2007 (**2007**) 040.

[42] A. Hoecker et al., TMVA 4—Toolkit for multivariate data analysis, arXiv:physics/0703039.

[43] M. Pivk and F. R. Le Diberder, sPlot: A statistical tool to unfold data distributions, Nucl. Instrum. Methods Phys. Res., Sect. A **555**, 356 (2005).

[44] T. Skwarnicki, A study of the radiative CASCADE transitions between the Upsilon-Prime and Upsilon resonances, Ph.D. thesis, Institute of Nuclear Physics, 1986.

[45] R. A. Fisher, The use of multiple measurements in taxonomic problems, Annu Eugen. **7**, 179 (1936).

[46] P. Koppenburg, Statistical biases in measurements with multiple candidates, arXiv:1703.01128.

[47] A. Zupanc et al. (Belle Collaboration), Measurement of the Branching Fraction $\mathcal{B}(\Lambda_c^+ \to pK^-\pi^+)$, Phys. Rev. Lett. **113**, 042002 (2014).

[48] R. Aaij et al. (LHCb Collaboration), Measurement of the fragmentation fraction ratio f_s/f_d and its dependence on B meson kinematics, J. High Energy Phys. 04 (2013) 001; f_s/f_d value updated in CERN Report No. LHCb-CONF-2013-011, (2013).

[49] R. Aaij et al. (LHCb Collaboration), Study of the kinematic dependences of Λ_b^0 production in pp collisions and a measurement of the $\Lambda_b^0 \to \Lambda_c^+\pi^-$ branching fraction, J. High Energy Phys. 08 (**2014**) 143.

[50] A. Satpathy et al. (Belle Collaboration), Study of $\bar{B}^0 \to D^{*0}\pi^+\pi^-$ decays, Phys. Lett. B **553**, 159 (2003).

[51] K. S. Cranmer, Kernel estimation in high-energy physics, Comput. Phys. Commun. **136**, 198 (2001).

[52] F. James, MINUIT—Function minimization and error analysis, CERN Program Library Long Writeup D506, 1994, http://hep.fi.infn.it/minuit.pdf.

[53] W. Verkerke and D. P. Kirkby, The RooFit toolkit for data modeling, eConf **C0303241**, MOLT007 (2003).

[54] R. Aaij et al., The LHCb trigger and its performance in 2011, J. Instrum. **8**, P04022 (2013).

[55] A. Martin Sanchez, P. Robbe, and M.-H. Schune, Performances of the LHCb L0 Calorimeter trigger, CERN Report No. LHCb-PUB-2011-026, (2011).

[56] R. Aaij et al. (LHCb Collaboration), Measurement of CP violation parameters in $B^0 \to DK^{*0}$ decays, Phys. Rev. D **90**, 112002 (2014).

[57] R. Aaij et al. (LHCb Collaboration), Measurements of the branching fractions of the decays $B_s^0 \to D_s^\mp K^\pm$ and $B_s^0 \to D_s^-\pi^+$, J. High Energy Phys. 06 (2012) 115.

[58] J. P. Lees et al. (BABAR Collaboration), Branching fraction measurements of the color-suppressed decays $\bar{B}^0 \to D^{(*)0}\pi^0$, $D^{(*)0}\eta$, $D^{(*)0}\omega$, and $D^{(*)0}\eta'$ and measurement of the polarization in the decay $\bar{B}^0 \to D^{*0}\omega$, Phys. Rev. D **84**, 112007 (2011); Erratum, Phys. Rev. D **87**, 039901(E) (2013).

[59] D. Matvienko et al. (Belle Collaboration), Study of D^{**} production and light hadronic states in the $\bar{B}^0 \to D^{*+}\omega\pi^-$ decay, Phys. Rev. D **92**, 012013 (2015).

[60] S. E. Csorna et al. (CLEO Collaboration), Measurements of the branching fractions and helicity amplitudes in $B \to D^*\rho$ decays, Phys. Rev. D **67**, 112002 (2003).

[61] B. Aubert et al. (BABAR Collaboration), Measurement of the Branching Fraction and Polarization for the Decay $B^- \to D^{0*}K^{*-}$, Phys. Rev. Lett. **92**, 141801 (2004).

[62] R. Aaij et al. (LHCb Collaboration), Observation of Overlapping Spin-1 and Spin-3 $\bar{D}^0K^-$ Resonances at Mass 2.86 GeV/c^2, Phys. Rev. Lett. **113**, 162001 (2014).

R. Aaij,[27] B. Adeva,[41] M. Adinolfi,[48] C. A. Aidala,[73] Z. Ajaltouni,[5] S. Akar,[59] P. Albicocco,[18] J. Albrecht,[10] F. Alessio,[42] M. Alexander,[53] A. Alfonso Albero,[40] S. Ali,[27] G. Alkhazov,[33] P. Alvarez Cartelle,[55] A. A. Alves Jr.,[59] S. Amato,[2] S. Amerio,[23] Y. Amhis,[7] L. An,[3] L. Anderlini,[17] G. Andreassi,[43] M. Andreotti,[16,a] J. E. Andrews,[60] R. B. Appleby,[56] F. Archilli,[27] P. d'Argent,[12] J. Arnau Romeu,[6] A. Artamonov,[39] M. Artuso,[61] K. Arzymatov,[37] E. Aslanides,[6] M. Atzeni,[44] S. Bachmann,[12] J. J. Back,[50] S. Baker,[55] V. Balagura,[7,b] W. Baldini,[16] A. Baranov,[37] R. J. Barlow,[56] S. Barsuk,[7] W. Barter,[56] F. Baryshnikov,[70] V. Batozskaya,[31] B. Batsukh,[61] V. Battista,[43] A. Bay,[43] J. Beddow,[53] F. Bedeschi,[24] I. Bediaga,[1] A. Beiter,[61] L. J. Bel,[27] N. Beliy,[63] V. Bellee,[43] N. Belloli,[20,c] K. Belous,[39] I. Belyaev,[34,42] E. Ben-Haim,[8] G. Bencivenni,[18] S. Benson,[27] S. Beranek,[9] A. Berezhnoy,[35] R. Bernet,[44] D. Berninghoff,[12] E. Bertholet,[8] A. Bertolin,[23] C. Betancourt,[44] F. Betti,[15,42] M. O. Bettler,[49] M. van Beuzekom,[27] Ia. Bezshyiko,[44] S. Bifani,[47] P. Billoir,[8] A. Birnkraut,[10] A. Bizzeti,[17,d] M. Bjørn,[57] T. Blake,[50] F. Blanc,[43] S. Blusk,[61] D. Bobulska,[53] V. Bocci,[26] O. Boente Garcia,[41] T. Boettcher,[58] A. Bondar,[38,e] N. Bondar,[33] S. Borghi,[56,42] M. Borisyak,[37] M. Borsato,[41,42] F. Bossu,[7] M. Boubdir,[9] T. J. V. Bowcock,[54] C. Bozzi,[16,42] S. Braun,[12] M. Brodski,[42] J. Brodzicka,[29] D. Brundu,[22] E. Buchanan,[48] A. Buonaura,[44] C. Burr,[56] A. Bursche,[22] J. Buytaert,[42] W. Byczynski,[42] S. Cadeddu,[22] H. Cai,[64] R. Calabrese,[16,a] R. Calladine,[47] M. Calvi,[20,c] M. Calvo Gomez,[40,f] A. Camboni,[40,f] P. Campana,[18] D. H. Campora Perez,[42] L. Capriotti,[56] A. Carbone,[15,g] G. Carboni,[25] R. Cardinale,[19,h] A. Cardini,[22] P. Carniti,[20,c] L. Carson,[52] K. Carvalho Akiba,[2] G. Casse,[54] L. Cassina,[20] M. Cattaneo,[42] G. Cavallero,[19,h]

R. Cenci,[24,i] D. Chamont,[7] M. G. Chapman,[48] M. Charles,[8] Ph. Charpentier,[42] G. Chatzikonstantinidis,[47] M. Chefdeville,[4] V. Chekalina,[37] C. Chen,[3] S. Chen,[22] S.-G. Chitic,[42] V. Chobanova,[41] M. Chrzaszcz,[42] A. Chubykin,[33] P. Ciambrone,[18] X. Cid Vidal,[41] G. Ciezarek,[42] P. E. L. Clarke,[52] M. Clemencic,[42] H. V. Cliff,[49] J. Closier,[42] V. Coco,[42] J. Cogan,[6] E. Cogneras,[5] L. Cojocariu,[32] P. Collins,[42] T. Colombo,[42] A. Comerma-Montells,[12] A. Contu,[22] G. Coombs,[42] S. Coquereau,[40] G. Corti,[42] M. Corvo,[16,a] C. M. Costa Sobral,[50] B. Couturier,[42] G. A. Cowan,[52] D. C. Craik,[58] A. Crocombe,[50] M. Cruz Torres,[1] R. Currie,[52] C. D'Ambrosio,[42] F. Da Cunha Marinho,[2] C. L. Da Silva,[74] E. Dall'Occo,[27] J. Dalseno,[48] A. Danilina,[34] A. Davis,[3] O. De Aguiar Francisco,[42] K. De Bruyn,[42] S. De Capua,[56] M. De Cian,[43] J. M. De Miranda,[1] L. De Paula,[2] M. De Serio,[14,j] P. De Simone,[18] C. T. Dean,[53] D. Decamp,[4] L. Del Buono,[8] B. Delaney,[49] H.-P. Dembinski,[11] M. Demmer,[10] A. Dendek,[30] D. Derkach,[37] O. Deschamps,[5] F. Dettori,[54] B. Dey,[65] A. Di Canto,[42] P. Di Nezza,[18] S. Didenko,[70] H. Dijkstra,[42] F. Dordei,[42] M. Dorigo,[42,k] A. Dosil Suárez,[41] L. Douglas,[53] A. Dovbnya,[45] K. Dreimanis,[54] L. Dufour,[27] G. Dujany,[8] P. Durante,[42] J. M. Durham,[74] D. Dutta,[56] R. Dzhelyadin,[39] M. Dziewiecki,[12] A. Dziurda,[42] A. Dzyuba,[33] S. Easo,[51] U. Egede,[55] V. Egorychev,[34] S. Eidelman,[38,e] S. Eisenhardt,[52] U. Eitschberger,[10] R. Ekelhof,[10] L. Eklund,[53] S. Ely,[61] A. Ene,[32] S. Escher,[9] S. Esen,[27] H. M. Evans,[49] T. Evans,[57] A. Falabella,[15] N. Farley,[47] S. Farry,[54] D. Fazzini,[20,42,c] L. Federici,[25] G. Fernandez,[40] P. Fernandez Declara,[42] A. Fernandez Prieto,[41] F. Ferrari,[15] L. Ferreira Lopes,[43] F. Ferreira Rodrigues,[2] M. Ferro-Luzzi,[42] S. Filippov,[36] R. A. Fini,[14] M. Fiorini,[16,a] M. Firlej,[30] C. Fitzpatrick,[43] T. Fiutowski,[30] F. Fleuret,[7,b] M. Fontana,[22,42] F. Fontanelli,[19,h] R. Forty,[42] V. Franco Lima,[54] M. Frank,[42] C. Frei,[42] J. Fu,[21,l] W. Funk,[42] C. Färber,[42] M. Féo Pereira Rivello Carvalho,[27] E. Gabriel,[52] A. Gallas Torreira,[41] D. Galli,[15,g] S. Gallorini,[23] S. Gambetta,[52] M. Gandelman,[2] P. Gandini,[21] Y. Gao,[3] L. M. Garcia Martin,[72] B. Garcia Plana,[41] J. García Pardiñas,[44] J. Garra Tico,[49] L. Garrido,[40] D. Gascon,[40] C. Gaspar,[42] L. Gavardi,[10] G. Gazzoni,[5] D. Gerick,[12] E. Gersabeck,[56] M. Gersabeck,[56] T. Gershon,[50] Ph. Ghez,[4] S. Gianì,[43] V. Gibson,[49] O. G. Girard,[43] L. Giubega,[32] K. Gizdov,[52] V. V. Gligorov,[8] D. Golubkov,[34] A. Golutvin,[55,70] A. Gomes,[1,m] I. V. Gorelov,[35] C. Gotti,[20,c] E. Govorkova,[27] J. P. Grabowski,[12] R. Graciani Diaz,[40] L. A. Granado Cardoso,[42] E. Graugés,[40] E. Graverini,[44] G. Graziani,[17] A. Grecu,[32] R. Greim,[27] P. Griffith,[22] L. Grillo,[56] L. Gruber,[42] B. R. Gruberg Cazon,[57] O. Grünberg,[67] C. Gu,[3] E. Gushchin,[36] Yu. Guz,[39,42] T. Gys,[42] C. Göbel,[62] T. Hadavizadeh,[57] C. Hadjivasiliou,[5] G. Haefeli,[43] C. Haen,[42] S. C. Haines,[49] B. Hamilton,[60] X. Han,[12] T. H. Hancock,[57] S. Hansmann-Menzemer,[12] N. Harnew,[57] S. T. Harnew,[48] C. Hasse,[42] M. Hatch,[42] J. He,[63] M. Hecker,[55] K. Heinicke,[10] A. Heister,[9] K. Hennessy,[54] L. Henry,[72] E. van Herwijnen,[42] M. Heß,[67] A. Hicheur,[2] D. Hill,[57] M. Hilton,[56] P. H. Hopchev,[43] W. Hu,[65] W. Huang,[63] Z. C. Huard,[59] W. Hulsbergen,[27] T. Humair,[55] M. Hushchyn,[37] D. Hutchcroft,[54] D. Hynds,[27] P. Ibis,[10] M. Idzik,[30] P. Ilten,[47] K. Ivshin,[33] R. Jacobsson,[42] J. Jalocha,[57] E. Jans,[27] A. Jawahery,[60] F. Jiang,[3] M. John,[57] D. Johnson,[42] C. R. Jones,[49] C. Joram,[42] B. Jost,[42] N. Jurik,[57] S. Kandybei,[45] M. Karacson,[42] J. M. Kariuki,[48] S. Karodia,[53] N. Kazeev,[37] M. Kecke,[12] F. Keizer,[49] M. Kelsey,[61] M. Kenzie,[49] T. Ketel,[28] E. Khairullin,[37] B. Khanji,[12] C. Khurewathanakul,[43] K. E. Kim,[61] T. Kirn,[9] S. Klaver,[18] K. Klimaszewski,[31] T. Klimkovich,[11] S. Koliiev,[46] M. Kolpin,[12] R. Kopecna,[12] P. Koppenburg,[27] S. Kotriakhova,[33] M. Kozeiha,[5] L. Kravchuk,[36] M. Kreps,[50] F. Kress,[55] P. Krokovny,[38,e] W. Krupa,[30] W. Krzemien,[31] W. Kucewicz,[29,n] M. Kucharczyk,[29] V. Kudryavtsev,[38,e] A. K. Kuonen,[43] T. Kvaratskheliya,[34,42] D. Lacarrere,[42] G. Lafferty,[56] A. Lai,[22] D. Lancierini,[44] G. Lanfranchi,[18] C. Langenbruch,[9] T. Latham,[50] C. Lazzeroni,[47] R. Le Gac,[6] A. Leflat,[35] J. Lefrançois,[7] R. Lefèvre,[5] F. Lemaitre,[42] O. Leroy,[6] T. Lesiak,[29] B. Leverington,[12] P.-R. Li,[63] T. Li,[3] Z. Li,[61] X. Liang,[61] T. Likhomanenko,[69] R. Lindner,[42] F. Lionetto,[44] V. Lisovskyi,[7] X. Liu,[3] D. Loh,[50] A. Loi,[22] I. Longstaff,[53] J. H. Lopes,[2] D. Lucchesi,[23,o] M. Lucio Martinez,[41] A. Lupato,[23] E. Luppi,[16,a] O. Lupton,[42] A. Lusiani,[24] X. Lyu,[63] F. Machefert,[7] F. Maciuc,[32] V. Macko,[43] P. Mackowiak,[10] S. Maddrell-Mander,[48] O. Maev,[33,42] K. Maguire,[56] D. Maisuzenko,[33] M. W. Majewski,[30] S. Malde,[57] B. Malecki,[29] A. Malinin,[69] T. Maltsev,[38,e] G. Manca,[22,p] G. Mancinelli,[6] D. Marangotto,[21,l] J. Maratas,[5,q] J. F. Marchand,[4] U. Marconi,[15] C. Marin Benito,[40] M. Marinangeli,[43] P. Marino,[43] J. Marks,[12] G. Martellotti,[26] M. Martin,[6] M. Martinelli,[43] D. Martinez Santos,[41] F. Martinez Vidal,[72] A. Massafferri,[1] R. Matev,[42] A. Mathad,[50] Z. Mathe,[42] C. Matteuzzi,[20] A. Mauri,[44] E. Maurice,[7,b] B. Maurin,[43] A. Mazurov,[47] M. McCann,[55,42] A. McNab,[56] R. McNulty,[13] J. V. Mead,[54] B. Meadows,[59] C. Meaux,[6] F. Meier,[10] N. Meinert,[67] D. Melnychuk,[31] M. Merk,[27] A. Merli,[21,l] E. Michielin,[23] D. A. Milanes,[66] E. Millard,[50] M.-N. Minard,[4] L. Minzoni,[16,a] D. S. Mitzel,[12] A. Mogini,[8] J. Molina Rodriguez,[1,r] T. Mombächer,[10] I. A. Monroy,[66] S. Monteil,[5] M. Morandin,[23] G. Morello,[18] M. J. Morello,[24,s] O. Morgunova,[69] J. Moron,[30] A. B. Morris,[6] R. Mountain,[61] F. Muheim,[52] M. Mulder,[27] D. Müller,[42] J. Müller,[10] K. Müller,[44] V. Müller,[10] P. Naik,[48] T. Nakada,[43] R. Nandakumar,[51] A. Nandi,[57] T. Nanut,[43] I. Nasteva,[2] M. Needham,[52] N. Neri,[21] S. Neubert,[12] N. Neufeld,[42] M. Neuner,[12] T. D. Nguyen,[43] C. Nguyen-Mau,[43,t] S. Nieswand,[9] R. Niet,[10] N. Nikitin,[35] A. Nogay,[69] D. P. O'Hanlon,[15]

A. Oblakowska-Mucha,[30] V. Obraztsov,[39] S. Ogilvy,[18] R. Oldeman,[22,p] C. J. G. Onderwater,[68] A. Ossowska,[29] J. M. Otalora Goicochea,[2] P. Owen,[44] A. Oyanguren,[72] P. R. Pais,[43] A. Palano,[14] M. Palutan,[18,42] G. Panshin,[71] A. Papanestis,[51] M. Pappagallo,[52] L. L. Pappalardo,[16,a] W. Parker,[60] C. Parkes,[56] G. Passaleva,[17,42] A. Pastore,[14] M. Patel,[55] C. Patrignani,[15,g] A. Pearce,[42] A. Pellegrino,[27] G. Penso,[26] M. Pepe Altarelli,[42] S. Perazzini,[42] D. Pereima,[34] P. Perret,[5] L. Pescatore,[43] K. Petridis,[48] A. Petrolini,[19,h] A. Petrov,[69] M. Petruzzo,[21,l] B. Pietrzyk,[4] G. Pietrzyk,[43] M. Pikies,[29] D. Pinci,[26] J. Pinzino,[42] F. Pisani,[42] A. Pistone,[19,h] A. Piucci,[12] V. Placinta,[32] S. Playfer,[52] J. Plews,[47] M. Plo Casasus,[41] F. Polci,[8] M. Poli Lener,[18] A. Poluektov,[50] N. Polukhina,[70,u] I. Polyakov,[61] E. Polycarpo,[2] G. J. Pomery,[48] S. Ponce,[42] A. Popov,[39] D. Popov,[47,11] S. Poslavskii,[39] C. Potterat,[2] E. Price,[48] J. Prisciandaro,[41] C. Prouve,[48] V. Pugatch,[46] A. Puig Navarro,[44] H. Pullen,[57] G. Punzi,[24,i] W. Qian,[63] J. Qin,[63] R. Quagliani,[8] B. Quintana,[5] B. Rachwal,[30] J. H. Rademacker,[48] M. Rama,[24] M. Ramos Pernas,[41] M. S. Rangel,[2] F. Ratnikov,[37,v] G. Raven,[28] M. Ravonel Salzgeber,[42] M. Reboud,[4] F. Redi,[43] S. Reichert,[10] A. C. dos Reis,[1] F. Reiss,[8] C. Remon Alepuz,[72] Z. Ren,[3] V. Renaudin,[7] S. Ricciardi,[51] S. Richards,[48] K. Rinnert,[54] P. Robbe,[7] A. Robert,[8] A. B. Rodrigues,[43] E. Rodrigues,[59] J. A. Rodriguez Lopez,[66] A. Rogozhnikov,[37] S. Roiser,[42] A. Rollings,[57] V. Romanovskiy,[39] A. Romero Vidal,[41] M. Rotondo,[18] M. S. Rudolph,[61] T. Ruf,[42] J. Ruiz Vidal,[72] J. J. Saborido Silva,[41] N. Sagidova,[33] B. Saitta,[22,p] V. Salustino Guimaraes,[62] C. Sanchez Gras,[27] C. Sanchez Mayordomo,[72] B. Sanmartin Sedes,[41] R. Santacesaria,[26] C. Santamarina Rios,[41] M. Santimaria,[18] E. Santovetti,[25,w] G. Sarpis,[56] A. Sarti,[18,x] C. Satriano,[26,y] A. Satta,[25] M. Saur,[63] D. Savrina,[34,35] S. Schael,[9] M. Schellenberg,[10] M. Schiller,[53] H. Schindler,[42] M. Schmelling,[11] T. Schmelzer,[10] B. Schmidt,[42] O. Schneider,[43] A. Schopper,[42] H. F. Schreiner,[59] M. Schubiger,[43] M. H. Schune,[7] R. Schwemmer,[42] B. Sciascia,[18] A. Sciubba,[26,x] A. Semennikov,[34] E. S. Sepulveda,[8] A. Sergi,[47,42] N. Serra,[44] J. Serrano,[6] L. Sestini,[23] P. Seyfert,[42] M. Shapkin,[39] Y. Shcheglov,[33,†] T. Shears,[54] L. Shekhtman,[38,e] V. Shevchenko,[69] E. Shmanin,[70] B. G. Siddi,[16] R. Silva Coutinho,[44] L. Silva de Oliveira,[2] G. Simi,[23,o] S. Simone,[14,j] N. Skidmore,[12] T. Skwarnicki,[61] E. Smith,[9] I. T. Smith,[52] M. Smith,[55] M. Soares,[15] l. Soares Lavra,[1] M. D. Sokoloff,[59] F. J. P. Soler,[53] B. Souza De Paula,[2] B. Spaan,[10] P. Spradlin,[53] F. Stagni,[42] M. Stahl,[12] S. Stahl,[42] P. Stefko,[43] S. Stefkova,[55] O. Steinkamp,[44] S. Stemmle,[12] O. Stenyakin,[39] M. Stepanova,[33] H. Stevens,[10] S. Stone,[61] B. Storaci,[44] S. Stracka,[24,i] M. E. Stramaglia,[43] M. Straticiuc,[32] U. Straumann,[44] S. Strokov,[71] J. Sun,[3] L. Sun,[64] K. Swientek,[30] V. Syropoulos,[28] T. Szumlak,[30] M. Szymanski,[63] S. T'Jampens,[4] Z. Tang,[3] A. Tayduganov,[6] T. Tekampe,[10] G. Tellarini,[16] F. Teubert,[42] E. Thomas,[42] J. van Tilburg,[27] M. J. Tilley,[55] V. Tisserand,[5] M. Tobin,[43] S. Tolk,[42] L. Tomassetti,[16,a] D. Tonelli,[24] D. Y. Tou,[8] R. Tourinho Jadallah Aoude,[1] E. Tournefier,[4] M. Traill,[53] M. T. Tran,[43] A. Trisovic,[49] A. Tsaregorodtsev,[6] A. Tully,[49] N. Tuning,[27,42] A. Ukleja,[31] A. Usachov,[7] A. Ustyuzhanin,[37] U. Uwer,[12] C. Vacca,[22,p] A. Vagner,[71] V. Vagnoni,[15] A. Valassi,[42] S. Valat,[42] G. Valenti,[15] R. Vazquez Gomez,[42] P. Vazquez Regueiro,[41] S. Vecchi,[16] M. van Veghel,[27] J. J. Velthuis,[48] M. Veltri,[17,z] G. Veneziano,[57] A. Venkateswaran,[61] T. A. Verlage,[9] M. Vernet,[5] M. Vesterinen,[57] J. V. Viana Barbosa,[42] D. Vieira,[63] M. Vieites Diaz,[41] H. Viemann,[67] X. Vilasis-Cardona,[40,f] A. Vitkovskiy,[27] M. Vitti,[49] V. Volkov,[35] A. Vollhardt,[44] B. Voneki,[42] A. Vorobyev,[33] V. Vorobyev,[38,e] C. Voß,[9] J. A. de Vries,[27] C. Vázquez Sierra,[27] R. Waldi,[67] J. Walsh,[24] J. Wang,[61] M. Wang,[3] Y. Wang,[65] Z. Wang,[44] D. R. Ward,[49] H. M. Wark,[54] N. K. Watson,[47] D. Websdale,[55] A. Weiden,[44] C. Weisser,[58] M. Whitehead,[9] J. Wicht,[50] G. Wilkinson,[57] M. Wilkinson,[61] M. R. J. Williams,[56] M. Williams,[58] T. Williams,[47] F. F. Wilson,[51,42] J. Wimberley,[60] M. Winn,[7] J. Wishahi,[10] W. Wislicki,[31] M. Witek,[29] G. Wormser,[7] S. A. Wotton,[49] K. Wyllie,[42] D. Xiao,[65] Y. Xie,[65] A. Xu,[3] M. Xu,[65] Q. Xu,[63] Z. Xu,[3] Z. Xu,[4] Z. Yang,[3] Z. Yang,[60] Y. Yao,[61] H. Yin,[65] J. Yu,[65,aa] X. Yuan,[61] O. Yushchenko,[39] K. A. Zarebski,[47] M. Zavertyaev,[11,u] D. Zhang,[65] L. Zhang,[3] W. C. Zhang,[3,bb] Y. Zhang,[7] A. Zhelezov,[12] Y. Zheng,[63] X. Zhu,[3] V. Zhukov,[9,35] J. B. Zonneveld,[52] and S. Zucchelli[15]

(LHCb Collaboration)

[1]Centro Brasileiro de Pesquisas Físicas (CBPF), Rio de Janeiro, Brazil
[2]Universidade Federal do Rio de Janeiro (UFRJ), Rio de Janeiro, Brazil
[3]Center for High Energy Physics, Tsinghua University, Beijing, China
[4]Université Grenoble Alpes, Université Savoie Mont Blanc, CNRS, IN2P3-LAPP, Annecy, France
[5]Clermont Université, Université Blaise Pascal, CNRS/IN2P3, LPC, Clermont-Ferrand, France
[6]Aix Marseille Université, CNRS/IN2P3, CPPM, Marseille, France
[7]LAL, Université Paris-Sud, CNRS/IN2P3, Université Paris-Saclay, Orsay, France
[8]LPNHE, Sorbonne Université, Paris Diderot Sorbonne Paris Cité, CNRS/IN2P3, Paris, France
[9]I. Physikalisches Institut, RWTH Aachen University, Aachen, Germany

[10]*Fakultät Physik, Technische Universität Dortmund, Dortmund, Germany*
[11]*Max-Planck-Institut für Kernphysik (MPIK), Heidelberg, Germany*
[12]*Physikalisches Institut, Ruprecht-Karls-Universität Heidelberg, Heidelberg, Germany*
[13]*School of Physics, University College Dublin, Dublin, Ireland*
[14]*INFN Sezione di Bari, Bari, Italy*
[15]*INFN Sezione di Bologna, Bologna, Italy*
[16]*INFN Sezione di Ferrara, Ferrara, Italy*
[17]*INFN Sezione di Firenze, Firenze, Italy*
[18]*INFN Laboratori Nazionali di Frascati, Frascati, Italy*
[19]*INFN Sezione di Genova, Genova, Italy*
[20]*INFN Sezione di Milano-Bicocca, Milano, Italy*
[21]*INFN Sezione di Milano, Milano, Italy*
[22]*INFN Sezione di Cagliari, Monserrato, Italy*
[23]*INFN Sezione di Padova, Padova, Italy*
[24]*INFN Sezione di Pisa, Pisa, Italy*
[25]*INFN Sezione di Roma Tor Vergata, Roma, Italy*
[26]*INFN Sezione di Roma La Sapienza, Roma, Italy*
[27]*Nikhef National Institute for Subatomic Physics, Amsterdam, Netherlands*
[28]*Nikhef National Institute for Subatomic Physics and VU University Amsterdam, Amsterdam, Netherlands*
[29]*Henryk Niewodniczanski Institute of Nuclear Physics Polish Academy of Sciences, Kraków, Poland*
[30]*AGH - University of Science and Technology, Faculty of Physics and Applied Computer Science,
Kraków, Poland*
[31]*National Center for Nuclear Research (NCBJ), Warsaw, Poland*
[32]*Horia Hulubei National Institute of Physics and Nuclear Engineering, Bucharest-Magurele, Romania*
[33]*Petersburg Nuclear Physics Institute (PNPI), Gatchina, Russia*
[34]*Institute of Theoretical and Experimental Physics (ITEP), Moscow, Russia*
[35]*Institute of Nuclear Physics, Moscow State University (SINP MSU), Moscow, Russia*
[36]*Institute for Nuclear Research of the Russian Academy of Sciences (INR RAS), Moscow, Russia*
[37]*Yandex School of Data Analysis, Moscow, Russia*
[38]*Budker Institute of Nuclear Physics (SB RAS), Novosibirsk, Russia*
[39]*Institute for High Energy Physics (IHEP), Protvino, Russia*
[40]*ICCUB, Universitat de Barcelona, Barcelona, Spain*
[41]*Instituto Galego de Física de Altas Enerxías (IGFAE), Universidade de Santiago de Compostela,
Santiago de Compostela, Spain*
[42]*European Organization for Nuclear Research (CERN), Geneva, Switzerland*
[43]*Institute of Physics, Ecole Polytechnique Fédérale de Lausanne (EPFL), Lausanne, Switzerland*
[44]*Physik-Institut, Universität Zürich, Zürich, Switzerland*
[45]*NSC Kharkiv Institute of Physics and Technology (NSC KIPT), Kharkiv, Ukraine*
[46]*Institute for Nuclear Research of the National Academy of Sciences (KINR), Kyiv, Ukraine*
[47]*University of Birmingham, Birmingham, United Kingdom*
[48]*H.H. Wills Physics Laboratory, University of Bristol, Bristol, United Kingdom*
[49]*Cavendish Laboratory, University of Cambridge, Cambridge, United Kingdom*
[50]*Department of Physics, University of Warwick, Coventry, United Kingdom*
[51]*STFC Rutherford Appleton Laboratory, Didcot, United Kingdom*
[52]*School of Physics and Astronomy, University of Edinburgh, Edinburgh, United Kingdom*
[53]*School of Physics and Astronomy, University of Glasgow, Glasgow, United Kingdom*
[54]*Oliver Lodge Laboratory, University of Liverpool, Liverpool, United Kingdom*
[55]*Imperial College London, London, United Kingdom*
[56]*School of Physics and Astronomy, University of Manchester, Manchester, United Kingdom*
[57]*Department of Physics, University of Oxford, Oxford, United Kingdom*
[58]*Massachusetts Institute of Technology, Cambridge, Massachusetts, USA*
[59]*University of Cincinnati, Cincinnati, Ohio, USA*
[60]*University of Maryland, College Park, Maryland, USA*
[61]*Syracuse University, Syracuse, New York, USA*
[62]*Pontifícia Universidade Católica do Rio de Janeiro (PUC-Rio), Rio de Janeiro, Brazil
[associated with Institution Universidade Federal do Rio de Janeiro (UFRJ), Rio de Janeiro, Brazil]*
[63]*University of Chinese Academy of Sciences, Beijing, China
(associated with Institution Center for High Energy Physics, Tsinghua University, Beijing, China)*
[64]*School of Physics and Technology, Wuhan University, Wuhan, China
(associated with Institution Center for High Energy Physics, Tsinghua University, Beijing, China)*

[65]Institute of Particle Physics, Central China Normal University, Wuhan, Hubei, China
(associated with Institution Center for High Energy Physics, Tsinghua University, Beijing, China)
[66]Departamento de Fisica, Universidad Nacional de Colombia, Bogota, Colombia
(associated with Institution LPNHE, Sorbonne Université, Paris Diderot Sorbonne Paris Cité,
CNRS/IN2P3, Paris, France)
[67]Institut für Physik, Universität Rostock, Rostock, Germany
(associated with Institution Physikalisches Institut, Ruprecht-Karls-Universität Heidelberg,
Heidelberg, Germany)
[68]Van Swinderen Institute, University of Groningen, Groningen, Netherlands
(associated with Institution Nikhef National Institute for Subatomic Physics, Amsterdam, Netherlands)
[69]National Research Centre Kurchatov Institute, Moscow, Russia
[associated with Institution Institute of Theoretical and Experimental Physics (ITEP), Moscow, Russia]
[70]National University of Science and Technology "MISIS", Moscow, Russia
[associated with Institution Institute of Theoretical and Experimental Physics (ITEP), Moscow, Russia]
[71]National Research Tomsk Polytechnic University, Tomsk, Russia
[associated with Institution Institute of Theoretical and Experimental Physics (ITEP), Moscow, Russia]
[72]Instituto de Fisica Corpuscular, Centro Mixto Universidad de Valencia - CSIC, Valencia, Spain
(associated with Institution ICCUB, Universitat de Barcelona, Barcelona, Spain)
[73]University of Michigan, Ann Arbor, Michigan, USA
(associated with Institution Syracuse University, Syracuse, New York, USA)
[74]Los Alamos National Laboratory (LANL), Los Alamos, New Mexico, USA
(associated with Institution Syracuse University, Syracuse, New York, USA)

[†]Deceased.
[a]Also at Università di Ferrara, Ferrara, Italy.
[b]Also at Laboratoire Leprince-Ringuet, Palaiseau, France.
[c]Also at Università di Milano Bicocca, Milano, Italy.
[d]Also at Università di Modena e Reggio Emilia, Modena, Italy.
[e]Also at Novosibirsk State University, Novosibirsk, Russia.
[f]Also at LIFAELS, La Salle, Universitat Ramon Llull, Barcelona, Spain.
[g]Also at Università di Bologna, Bologna, Italy.
[h]Also at Università di Genova, Genova, Italy.
[i]Also at Università di Pisa, Pisa, Italy.
[j]Also at Università di Bari, Bari, Italy.
[k]Also at Sezione INFN di Trieste, Trieste, Italy.
[l]Also at Università degli Studi di Milano, Milano, Italy.
[m]Also at Universidade Federal do Triângulo Mineiro (UFTM), Uberaba-MG, Brazil.
[n]Also at AGH - University of Science and Technology, Faculty of Computer Science, Electronics and Telecommunications, Kraków, Poland.
[o]Also at Università di Padova, Padova, Italy.
[p]Also at Università di Cagliari, Cagliari, Italy.
[q]Also at MSU - Iligan Institute of Technology (MSU-IIT), Iligan, Philippines.
[r]Also at Escuela Agrícola Panamericana, San Antonio de Oriente, Honduras.
[s]Also at Scuola Normale Superiore, Pisa, Italy.
[t]Also at Hanoi University of Science, Hanoi, Vietnam.
[u]Also at P.N. Lebedev Physical Institute, Russian Academy of Science (LPI RAS), Moscow, Russia.
[v]Also at National Research University Higher School of Economics, Moscow, Russia.
[w]Also at Università di Roma Tor Vergata, Roma, Italy.
[x]Also at Università di Roma La Sapienza, Roma, Italy.
[y]Also at Università della Basilicata, Potenza, Italy.
[z]Also at Università di Urbino, Urbino, Italy.
[aa]Also at Physics and Micro Electronic College, Hunan University, Changsha City, China.
[bb]Also at School of Physics and Information Technology, Shaanxi Normal University (SNNU), Xi'an, China.